

# Graphene-Mediated Light-Matter Interaction

Thesis by  
Jeremy Jean Brouillet

In Partial Fulfillment of the Requirements for the  
Degree of  
Doctor of Philosophy

The logo for the California Institute of Technology (Caltech), featuring the word "Caltech" in a bold, orange, sans-serif font.

CALIFORNIA INSTITUTE OF TECHNOLOGY  
Pasadena, California

2019  
Defended May 17th, 2019

© 2019

Jeremy Jean Brouillet  
ORCID: 0000-0001-6664-5643

All rights reserved

*For Estelle.  
A loving grandmother who believed in education.*

## ACKNOWLEDGEMENTS

There are so many people I want to thank. It takes a village to get through a PhD, and I am truly appreciative of the support along the way. I am thankful for the wandering in this long journey, and am glad to have shared my time with so many wonderful people. People are the most important part of life.

First and foremost, I'd like to thank my family. You mean the world to me. Carol and Jean-Luc are the best parents in the whole wide world. My brothers, Daniel and Jules, have kept up my spirits and provided many laughs. Thanks for the nights of gaming and putting up with my wild antics over these many years. My extended family, thank you. I value the rare moments I get to spend with all of you. In particular, I'd like to thank my godparents, Élyse and Pierre, for their words of support and for keeping a nice-looking shirt on my back. Thank you to my grandfather François for teaching me that work can be hard, and sometimes, you just need to do it. I'd like to thank Grandma Janet for getting me out hiking, an activity that has brought in much-needed fresh air during graduate school. I'd like to thank my cousin, Dr. Keri Kuhn, who prevailed in her own journey to get a PhD in applied physics.

I'd like to thank my many friends in grad school. My rock for many years was our D&D group. Dan Brooks was an excellent roommate, a better friend, and a master Dominion guru. Dustin Anderson, thank you for the many good laughs we had in the apartment. Kevin Barkett, thanks for groaning at my profligate punning. Tony Bartolotta ran an excellent high-seas D&D game and let me take over the world. Jason Pollack, your games never ceased to amaze me as we trip over and into ourselves continually without fail. Jonathan Blackman, your good spirits always kept the energy up. Will Frankland plays the best deranged hermit I have ever known.

I'd like to thank the many many theater people I have known in my time at Caltech. Theater has always been a place of freedom, expression, a safety valve, and a place to experiment. There are far too many people to name and I want to thank everyone who's been with me in this journey. I'd particularly like to thank Brian Brophy, Cara King, Tiffany Kim, Cierena Marks, Penelope Chan, Grant Remmen, David Coren, David Hodge, Utkarsh Mital, Manan Arya, Giulia Pellegrino, Yaz Billeh, Elizabeth Freeman, Jake Mattinson, Chris Bell, Larissa Charnsangavej, Ed Brown,

GG Dhandapani, and Ben Sveinbjörnsson. Mark Kozlowski, thank you for always hitting the right note and helping me learn to sing. Zachary Abbott, thank you for your friendship and advice over the years. Todd Brun, you cast me in the first Caltech show I ever performed in, and it drew me into this wonderful family. I'd like to thank my new D&D group, Dave Seal, Ella Seal, Zach Tobin, and Ben Solish. I'm glad you enjoy the worlds I create, and thank you for bringing me into yours.

I'd like to thank my many friends across the Caltech community. Magnus Haw, you managed to make pasta too spicy for me, and are also one of the most creative and environmentally conscious physicists I have met. Yu-Hung Lai, thank you for doing the mammoth share of the driving on our road trips up to the Bay Area to visit our people, and also for being a great friend as we endured the rigors of grad school. Aaron Pearlman is an intense prolific physicist and I wish him and Sheri well. Sam Samuelson and Jason Allmaras, thank you for the many freewheeling discussions over frozen yogurt. I'd like to thank Alex Turzillo for being willing to try out wild backpacking routes with me, even if they involve scrambling up obscure peaks deep in the desert. Tal Einav has a wonderful upbeat spirit and is endlessly encouraging. Nicole Halpern is the most dedicated researcher I have ever met, and I'm glad she made the time for me in her juggernaut of a schedule. Rebecca Rojanksy and James Parle, thank you for the many good hikes we've enjoyed together. Brian He, thank you for the years of friendship, I wish you well. Alex Place, thank you for the good hikes and for your wild energy. Michael Seaman, may you do all the math and happy trails. Viki Chernow, thank you for your years of insight on the graduate experience.

I managed to briefly explore outside of Caltech and met many wonderful people as well, through a shared joy of swing dancing. Michele Webb, thank for the many dinners we cooked together. Kate Miller, your passion for your craft is ever inspiring. Evelyn Askew always brought a smile to my face on the dance floor. Jennifer Rogers, thank you for many good evenings of dancing and backpacking through deep canyons in the southwest. Joži McKiernan, I always enjoy nerding out with you. Lara Bideyan, thank you for getting me out running on a regular basis. Denise Machin, thank you for cheering me on in my doctoral journey and providing me with bountiful food.

I'd like to thank the dear friends from before Caltech began. Arman Boehm, Valentin Bonnet, and Ryan Kessler, you're the best of friends. Thank you for sticking with me through the decades, despite me being off in other parts of the country and the world. It's always a joy to see you guys, and here's to many more decades together.

I'd like to thank Oren Gazit, one of my oldest friends, who got me playing soccer and encouraged me to read. Sophie Chistel, Karen Reitman, Rahul Kerur, and Lukas Schleuniger, thank you for being good friends beyond the theater. I'd like to thank Jim Shelby for everything. I'd like to thank Stuart Kim, Elsa Garmire, and Jifeng Liu for bringing me into their labs and teaching me to do science. I'd like to thank Emi Weed for her words of encouragement as we navigated our graduate experiences.

I'd like to thank the many teachers in the Caltech community. Nancy Sulahian, thank you for teaching me to sing. Greg Fletcher, thank you for making the Caltech Y a wonderful place and for trusting me to take care of undergrads on backpacking trips on the far rims of civilization. George Rossman has been fantastically helpful, both for teaching me how to run a Fourier-transform infrared spectroscopy and how to do science. His door was always open and I appreciated his time, openness, patience, and enthusiasm. You rock!

I'd like to thank the many labmates over the years who have helped me. Jim Fakonas is the first friend I made in the Atwater lab. You're good people, Jim. I'd like to thank Krishnan Thyagarajan, the only labmate who I talked into going up a mountain with me and astonishingly, the one who wanted to keep hiking more of them. I'd like to thank Victor Brar and Michelle Sherrott for getting me started with graphene. I'd like to thank Georgia Papadakis, Pankaj Jha, and Souvik Biswas for their help on our science. Phillip Jahelka, thank you for keeping the computers running, and for fixing them when I ran overly ambitious simulations that ate up all the memory. Cris Flowers and Rebecca Glauddell, thank you for keeping us safe in lab. I'd like to thank my officemates over the years for good discussions, Ragip Pala, Ghazal Kafaie, Ognjen Ilic, and Hamid Akbari. A huge thank you to the KNI staff for keeping the tools up and running. In particular, I'd like to thank Alex Wertheim who helped me in my journey to master thin-film deposition. I'd also like to thank Guy DeRose, Matt Sullivan, Melissa Melendes, Nils Asplund, Nathan Lee, and Bert Mendoza for their help at with equipment acrosss the lab.

I'd like to thank my committee, Kerry Vahala, George Rossman, and Andrei Faraon. I appreciate you take the time to help me learn along the way. I'd like to thank Keith Schwab, who served on my candidacy committee. I'd like to thank my advisor, Harry Atwater, for his support over the years.

## ABSTRACT

Advances in 2D materials have opened a wealth of possibilities for the control of emission and propagation of light on length scales much smaller than the wavelength of light. Graphene, with highly-confined electrostatically tunable plasmons, provides a strong platform for explore a number of avenues.

We show that graphene that can increase the luminescence of erbium by 80%, can induce population inversion in a three-level system, speed up the response time by over an order of magnitude, and has modulation depth of up to 14 dB for luminescence.

We experimentally demonstrated a tunable epsilon-near-zero metamaterial with a elliptic-to-hyperbolic transition. The device had been theorized for many years and we provide the first experimental realization.

We explore the properties of an isotropic tunable 2D heterostructure composed of black phosphorus, hexagonal boron nitride, and graphene. These symmetry-breaking materials create an effective permittivity that is biaxially anisotropic and tunable. This material supports tunable beam steering based on propagation of energy along the hyperbolic dispersion lines.

## PUBLISHED CONTENT AND CONTRIBUTIONS

- [1] J. Brouillet, K. P. Jha, and A. A. Atwater. “Electrical modulation of emission from erbium ions coupled to graphene nanoribbons”. *In preparation* ().  
J.B. conceived the project, performed the simulations, analyzed the data, and wrote the manuscript.
- [2] J. Brouillet, G. T. Papadakis, and A. A. Atwater. “Experimental demonstration of tunable graphene hyperbolic metamaterial”. *In preparation* ().  
J.B. designed the heterostructure, fabricated the device, measured the device, and wrote the manuscript.

## TABLE OF CONTENTS

Acknowledgements . . . . .	iv
Abstract . . . . .	vii
Published Content and Contributions . . . . .	viii
Table of Contents . . . . .	ix
List of Illustrations . . . . .	xi
List of Tables . . . . .	xvi
Chapter I: Introduction . . . . .	1
1.1 Photonics . . . . .	1
1.2 Properties of graphene . . . . .	1
1.3 Hyperbolic metmaterials . . . . .	6
1.4 The Scope of this thesis . . . . .	7
Chapter II: Erbium Local Density of States Modification by Graphene . . . . .	8
2.1 Introduction . . . . .	8
2.2 System Overview: Graphene Ribbons on on $\text{Er}^{3+}:\text{Y}_2\text{O}_3$ . . . . .	9
2.3 Results and discussion: Enhancement of Luminescence . . . . .	14
2.4 Conclusions . . . . .	16
Chapter III: Experimental demonstration of tunable graphene hyperbolic metamaterial . . . . .	18
3.1 Introduction . . . . .	18
3.2 Fabrication Challenges . . . . .	19
3.3 $\text{SiO}_2/\text{Al}_2\text{O}_3/\text{Graphene}$ Heterostructure . . . . .	20
3.4 Effective permittivity via transfer matrices and parameter retrieval . . . . .	24
3.5 FITR Measurements of tunable permittivity . . . . .	25
3.6 Conclusions . . . . .	26
3.7 Methods: Fabrication . . . . .	26
3.8 Methods: Sample Characterization . . . . .	32
Chapter IV: Tuning the dispersion of anisotropic 2D materials with graphene . . . . .	39
4.1 Introduction . . . . .	39
4.2 Properties of black phosphorus . . . . .	39
4.3 Permittivity of BP . . . . .	40
4.4 Properties of hBN . . . . .	41
4.5 Design of a Graphene/BP Heterostructure . . . . .	41
4.6 Effective permittivity . . . . .	41
4.7 Near-field imaging of isofrequency contours . . . . .	43
4.8 FDTD Simulations . . . . .	45
4.9 Biaxial effective parameter retrieval . . . . .	46
4.10 Conclusion . . . . .	48
Chapter V: Perspectives and Future Works . . . . .	50
5.1 Graphene for light emission . . . . .	50

5.2 Tunable hyperbolic metamaterials . . . . .	51
5.3 Van Der Waals materials beyond graphene . . . . .	52
5.4 Conclusions . . . . .	52
Bibliography . . . . .	53

## LIST OF ILLUSTRATIONS

<i>Number</i>	<i>Page</i>
1.1 The Dirac Cone of graphene by the K point has linear dispersion. . .	2
1.2 The permittivity of the in-plane components of graphene. As the material is doped, the $\text{Re}(\epsilon)$ goes negative as the graphene acts as a metal. This negative $\text{Re}(\epsilon)$ enables graphene's plasmonic behavior. . .	5
2.1 (a) An $\text{Er}^{3+}$ ion in $\text{Y}_2\text{O}_3$ is excited by a 980 nm laser at distance $d$ to a 8 nm wide graphene nanoribbon. It emits at $2.74 \mu\text{m}$ for the ${}^4I_{11/2} \rightarrow {}^4I_{13/2}$ transition and 1535 nm for the ${}^4I_{13/2} \rightarrow {}^4I_{15/2}$ transition. (b) The three-level system of the $\text{Er}^{3+}$ couples to two graphene plasmons. The $\text{Er}^{3+}$ is pumped at $\Omega_0$ . The $2.74 \mu\text{m}$ transition occurs at rate $\gamma_{32}$ and depends on the graphene Fermi level and the distance between the emitter and the graphene ribbon. The $1.535 \mu\text{m}$ transition occurs at rate $\gamma_{32}$ . . . . .	9
2.2 The electric field $ E $ of the 8 nm graphene nanoribbon. The top perspective is viewed at a height of 20 nm and the side view is at a distance of 20 nm. It is excited by a $2.74 \mu\text{m}$ dipole 1 nm below the edge of the ribbon and supports plasmon of wavelength $\lambda_p = \lambda_0/93$ . . .	10
2.3 The relative transition rates for two different on-resonance ribbons widths for a dipole 12 nm from a 8 nm graphene ribbon. By modulating the Fermi level, we can control the transition rate at $2.74 \mu\text{m}$ as well as at 1535 nm. The black dashed lines indicate the transitions of the $\text{Er}^{3+}:\text{Y}_2\text{O}_3$ . The transition rate is relative to that of a dipole not next to graphene. . . . .	12
2.4 The radiative emission rate of a dipole position 1 nm above the metamaterial relative to a dipole with no graphene. The graphene Fermi level is varied to tune the relative couple of (a,b) 8 nm ribbons and (c,d) 20 nm graphene ribbons. (a,c) Plasmons near the ${}^4I_{11/2} \rightarrow {}^4I_{13/2}$ transition. (b,d) Plasmons near the ${}^4I_{13/2} \rightarrow {}^4I_{15/2}$ transition. . .	13

2.5	The population of the $^4I_{13/2}$ level is dependent on distance and the graphene Fermi level. The PL enhancement is the ratio of the graphene at $E_f=0.64$ eV to $E_f=0.0$ eV. By optimizing the distance to 12 nm, we can attain a high PL enhancement of 28 with pump powers under 10mW. . . . .	14
2.6	Steady-state luminescence $Er^{3+}$ ions coupled to on and off resonance graphene nanoribbons relative to $Er^{3+}$ emission with no graphene. Doping greatly increases the luminescence of $Er^{3+}$ relative from the $E_f=0$ to $E_f=0.64$ eV. Above 50mW, we show an overall increase in luminescence for heavily doped graphene. Beyond 300mW, we hit the optical damage threshold[69]. . . . .	15
2.7	Graphene nanoribbons more rapidly enhance the luminescence as they fill the $^4I_{13/2}$ state sooner than normal erbium. We assume an incident power of 0.3W. . . . .	16
3.1	Left: Schematic of a theoretical metamaterial stack. Right: Schematic of the fabricated individual device. The layers: Lightly-doped silicon substrate, thermally-grown $SiO_2$ , atomic layer deposited (ALD) $Al_2O_3$ , transferred chemical-vapor deposited (CVD) graphene, electron-beam evaporated Al, ALD $Al_2O_3$ , and plasma-enhance chemical vapor deposition $SiO_2$ . The thin layers of $Al_2O_3$ are necessary for feasibility fabrication. The thick $SiO_2$ contribute to the majority of the dielectric response. Contacts are added to gate and measure the resistance of the graphene. The graphene is tuned by gating against the back silicon substrate. . . . .	20
3.2	Material parameter retrieval is used on the ellipsometric data for $SiO_2$ and graphene to calculate effective $\epsilon_o$ that is tuned with an electrical bias over a range of Fermi levels from 0 to 0.5 eV. (a) Imaginary value of $\epsilon_o$ for the $SiO_2$ and overall structure. (b) Real part of $\epsilon_o$ . (c) Inset where the real part of $\epsilon_o$ crosses zero at a range of wavelengths depending on the $E_f$ . . . . .	21
3.3	(a) Absolute FTIR transmission over a range of Fermi levels. (b) Experimental data normalized to $E_f=0$ eV, the Dirac point. (c) Experiment compared with theory, based on ellipsometric fits of the thickness and optical properties constituent layers. Normalized to $E_f=0$ eV. Deviations arise due to hysteresis of the graphene induced by charge trapping. . . . .	23

3.4	Change of $\epsilon$ with applied bias. . . . .	25
3.5	A layer by layer depiction of the full graphene metmaterial stack, the layer thickness by two different modes of measurement, and the process used to create the layer. . . . .	27
3.6	An image of PMMA on graphene using a confocal microscope. (a) The graphene had been immersed in acetone for 45 minutes, but this did not remove all the PMMA, as shown by the orange patches. (b) The graphene with three acetone baths of 45 minutes . . . . .	28
3.7	Top SiO <sub>2</sub> delaminates from samples when deposited by e-beam evaporation. There is high thermal stress in a film deposited by e-beam evaporation. As the film cools, it causes stress in the film. The effects are visible to the naked eye. Graphene is the pale purple region and occupies most of the area save for the far left region. The blue wave lines are the delatminated regions. The delaminated region covers nearly the entire sheet of graphene. Delamination begins at a single point and spreads across the sample. It can occur a number of minutes after the device has left the e-beam chamber. If the device is left in the e-beam chamber in vacuum to slowly cool overnight, it will still delaminate. . . . .	31
3.8	A representative response of a sample under going electrical bias. Most samples were tested between -150V and 150V as they were liable to fail much beyond those voltage. There is a sharp increase in the leakage current under high bias. . . . .	33
3.9	(a) Applied bias versus graphene resistance after the graphene was transferred but before ALD. Note that the maximum resistance, the Dirac Peak, is at 180V. (b) Applied bias versus graphene resistance after aluminum metalization. The Dirac peak changes, from -60 V to 0 V due to hysteresis. The two lines represent the resistance measurement that was achieved immediately once hitting the voltage and after a minute of dwell time. Measurements were taken by moving 5 V once a minute and having a 5 minute dwell time at the maximum and minimum voltages. . . . .	34
3.10	(a) Graphene before PECVD (b) Graphene after PECVD. (c) Graphene after ozone-based ALD, an alternative approach not used in making the final sample. The additional peak indicates the presence of graphene oxide. . . . .	35

3.11	The ellipsometer fit of the ellipsometric model to the data for Si/SiO <sub>2</sub> . We see good agreement with the data. There are clear absorption lines of the SiO <sub>2</sub> near 8nm and 20nm due to phonos. . . . .	38
3.12	The ellipsometer fit of the model to the data for complete metamaterial, tuned to the Dirac Point. The fit MSE was 9.512. . . . .	38
4.1	The in-plane permittivity of black phosphorus[113]. $n$ is the carrier concentration. It exhibits tunable ENZ points. . . . .	40
4.2	A source above the graphene BP heterostructure excites in-plane plasmons. The graphene and BP are separated by a layer of hBN. Voltages $V_1$ and $V_2$ can be applied to electrostatically gate the graphene and BP.	42
4.3	The in-plane permittivities of the materials in the heterostructure and their effective permittivity. This structure is graphene at $E_f=0.1\text{eV}$ , 5 nm of hBN, 10 nm of BP with a carrier concentration $5\text{e}12$ , and 5 nm of hBN. . . . .	43
4.4	The in-plane effective permittivities for a variety of graphene Fermi levels. This structure is graphene with a Fermi level of 0.0 to 0.4V, 5 nm of hBN, 10 nm of BP with a carrier concentration $5\text{e}12$ , and 5 nm of hBN. . . . .	44
4.5	The in-plane effective permittivities for a variety of graphene Fermi levels. This structure is graphene with an $E_f$ of 0.1 eV, 5 nm of hBN, 10 nm of BP with a carrier concentration varying from $1\text{e}12$ to $9\text{e}12$ , and 5 nm of hBN. . . . .	45
4.6	The isofrequency curves of the simulation at $12\mu\text{m}$ The $E_f$ is 0.04 eV in (a) and increased up to 0.1 eV in (d). The red line is the dispersion of the BP and the green line is the dispersion of the heterostructure as a whole. As the the bias is applied, the area of isofrequencies flatten and expand as the isofrequency curves become more horizontal. . . .	46
4.7	(a-b) FFT image of the $E_z$ of a graphene-BP heterostructure at $\lambda = 12\mu\text{m}$ with a BP carrier concentration of $4\text{e}12\text{cm}^{-2}$ and a graphene Fermi level of (a) 0.1 eV (b) 0.2 eV. (c-d) Real space image of $ E $ of the above, indicating the direction of energy propagation. . . . .	47
4.8	The cross-sectional view of the electric field profile of a graphene-BP heterostructure taken 400 nm away from the dipole excitation. Graphene is at -53 nm, and BP is from -50 nm to 0 nm. This image shows that the majority of the power resides in the BP mode, but the highest electric field strength is in the underlying graphene sheet. . . .	48

- 4.9 Effective medium theory is used to calculate the angle of emission for a graphene-BP heterostructure at  $12\mu m$ . The thickness of the BP is 50 nm and is encapsulated in hBN. The graphene Fermi level  $E_f$  can control the beam angle, as can the BP carrier concentration. . . . 49

## LIST OF TABLES

<i>Number</i>		<i>Page</i>
4.1	FDTD Simulation Parameters Fig. 4.6 . . . . .	46

## *Chapter 1*

### INTRODUCTION

#### 1.1 Photonics

One of the first technologies humanity mastered was fire. From fire comes light. The nature of light has been continually studied for ages in order to understand what truly occurs. Classical optics covered the propagation of light through lens, telescopes, and other interactions with macroscopic objects. Looking at light on smaller and smaller scales, we go into the realm of photons. Photonics is the study of light on the nanoscale. It encompasses the generation of light, the manipulation of light as it propagates, and the eventual absorption of light. By controlling these nanoscale behaviors, we can govern the overall movement of light. Properties of optics are governed by Maxwell's equation [1]. We restrict our focus to source-free and current-free mediums and have the following set of equations:

$$\nabla \cdot \mathbf{D} = 0 \quad (1.1)$$

$$\nabla \cdot \mathbf{B} = 0 \quad (1.2)$$

$$\nabla \times \mathbf{E} = -\frac{\partial \mathbf{B}}{\partial t} \quad (1.3)$$

$$\nabla \times \mathbf{H} = \frac{1}{c^2} \frac{\partial \mathbf{D}}{\partial t} \quad (1.4)$$

#### 1.2 Properties of graphene

First isolated by Geim and Novoselov in their Nobel Prizing winning works[2], graphene has generated a massive amount of interest due to its unique properties. As a monolayer, it has a mode volume far below that of any 3D material, allowing for extreme confinement of modes. In addition, its properties depend on the charge carrier concentration, which can be electrostatically modulated. These two qualities are essential in the many projects described in this thesis. I explore the possibilities for controlling light with graphene.

There has been tremendous growth in the field in optoelectronics in the last decade due to graphene. A staggering number of publications have been written on graphene [3], covering a range of topics from synthesis [4, 5], to experimental properties and growth [6], to applications such as transistors [7], biocompatible materials [8],

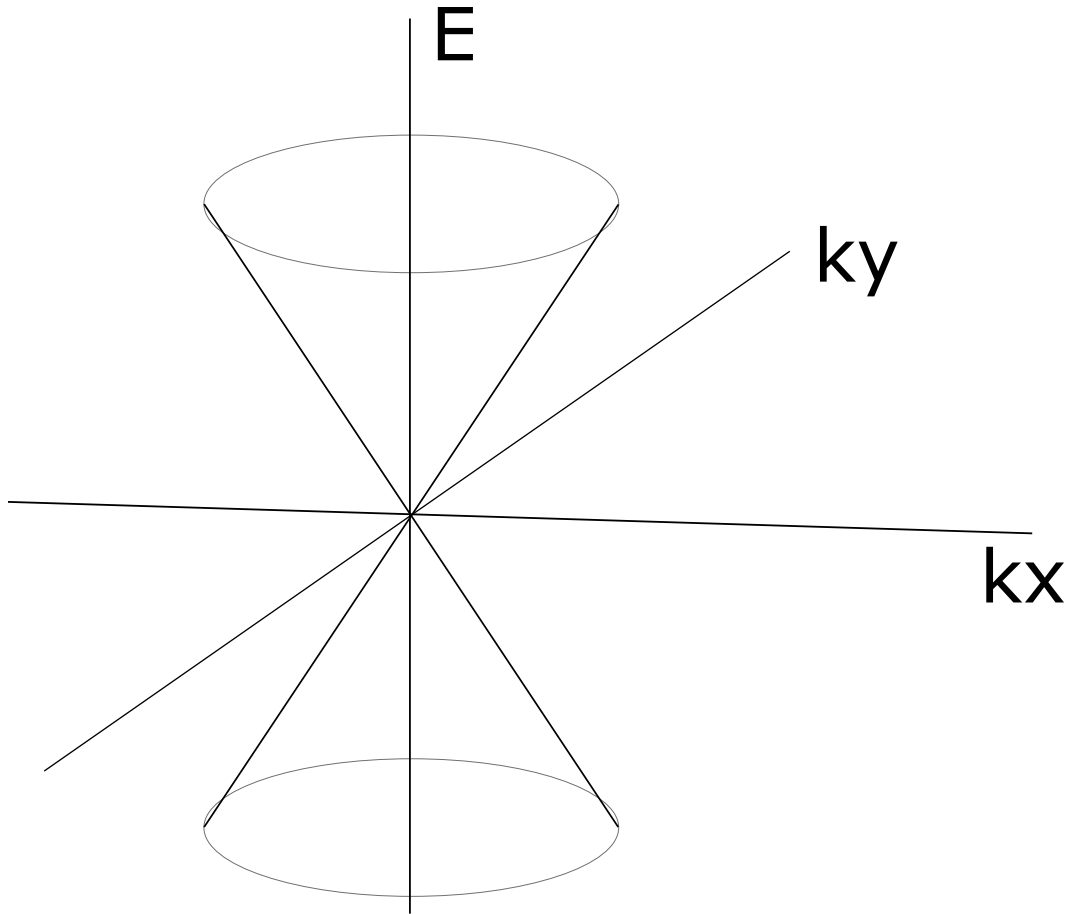


Figure 1.1: The Dirac Cone of graphene by the K point has linear dispersion.

photocatalysis [9], capacitors [10, 11], solar cells [12], batteries [13], and sensors [14]. Properties that have been explored include geometry [15, 16, 17], mechanics [18], thermal transport [19], doping [20], and defects [21].

Structurally, graphene is a hexagonal monolayer of carbon atoms. The carbon atoms have an  $sp^2$  hybridization, leaving the final electron free to make a high mobility  $\pi$  and  $\pi^*$  bond. This causes the electrons to act as a 2D electron gas, as they are confined in the out-of-plane direction but are free to propagate in plane. It is an excellent conductor of heat and is thermodynamically stable in air. It has excellent mechanical strength in-plane. It can be made through mechanical exfoliation from graphite or by growth in a furnace by chemical vapor deposition (CVD).

### **Electrical properties of graphene**

Graphene is a zero-overlap semimetal, meaning the valence and conduction bands do not overlap but instead touch at two points, K and K' of the Brillouin Zone.

About the K-points, graphene has a linear dispersion relation given [22]

$$E_s \mathbf{k} = s v |\mathbf{k}|. \quad (1.5)$$

In this equation,  $E$  is energy,  $\mathbf{k}$  is the wavevector,  $s = \pm 1$  for the valence (+1) and conduction (-1) bands, and  $v$  the Fermi velocity,  $10^6$  m/s. The effective electron mass relates to the curvature of the dispersion relation, so with a straight dispersion, the electron mass effectively goes to zero, leading to a "relativistic" effective mass  $m_c = E_f / \gamma^2$ , where  $\gamma$  is a band parameter close to the Fermi velocity. Due to the extremely low effective mass, graphene has excellent conductivity. Conductivity relates to the mobility of the graphene through

$$\sigma = e(n\mu_e + p\mu_h). \quad (1.6)$$

Here,  $\sigma$  is conductivity,  $e$  is the electron charge,  $n$  is the density of holes,  $p$  is the density of electrons,  $\mu_e$  is the mobility of electrons, and  $\mu_h$  is the mobility of holes. The mobility depends on the graphene scattering time. Scattering time depends on the quality of graphene. Practical values on graphene mobility can range from  $2,000 \frac{cm^2}{Vs}$  for CVD graphene to  $200,000 \frac{cm^2}{Vs}$  or even  $1,000,000 \frac{cm^2}{Vs}$  for exfoliated graphene [23, 24].

### Electrostatic doping of graphene

The Fermi level is the level at which at which the probability of occupation by an electron is 50%, as dictated by the Fermi-Dirac distribution. At low temperatures, this is the edge where the graphene goes from being filled with electrons to having no electrons. By apply a voltage between the graphene and gate, the graphene can be charged with either electrons or holes. The number of carriers in the graphene sets the Fermi level of the material.  $E_f \propto n^{1/2}$ . At the Dirac peak of the resistance, the Fermi level is zero and is known as the charge neutral point. It contains zero carrier density and is the point at which the Fermi level is aligned between the valence and conduction band.

### Optical properties of graphene

In the limit of zero temperature and no doping [25],

$$\sigma = \pi e^2 / (2h). \quad (1.7)$$

Absorption is  $\pi\alpha = 2.3\%$ , where  $\alpha = \frac{e^2}{\hbar c}$  is the fine structure constant. This is a fundamental value. At finite temperatures and non-zero doping, the optical properties becomes more complex.

Graphene absorption is due to intraband and interband effects. Intraband absorption is when the charge carriers are moved within the same band. These are lower energy behaviors and dominate in the infrared. These interband absorptions are due to the Drude-Boltzmann conductivity. The local Drude model describes the conductivity  $\sigma$  as a function of frequency and  $E_f$  [24]:

$$\sigma(\omega, E_f) = \frac{ie^2|E_f|}{\pi\hbar^2(\omega + i/\tau_\epsilon)}. \quad (1.8)$$

Interband absorption occurs at higher energy effect as electrons need to be excited from the conduction to valance band. As the graphene is doped, the valence band is filled. This filling of available states Paul blocks interband transitions. This interband Pauli blocking occurs for  $\omega < 2E_f$ , where  $\omega$  is the angular frequency and  $E_f$  is the Fermi level of the graphene.

The optical surface conductivity can be calculated from the Kubo formula [26]:

$$\sigma(\omega, \mu_c, \Gamma, T) = \frac{je^2(\omega - j2\Gamma)}{\pi\hbar^2} \left[ \frac{1}{(\omega - j2\Gamma)^2} \int_0^\infty \epsilon \left( \frac{\partial f_d(\epsilon)}{\partial \epsilon} - \frac{\partial f_d(-\epsilon)}{\partial \epsilon} \right) d\epsilon - \int_0^\infty \frac{f_d(-\epsilon) - f_d(\epsilon)}{(\omega - j2\Gamma)^2 - 4(\epsilon/\hbar)^2} d\epsilon \right],$$

where  $\hbar$  is the reduced Plank's constant,  $f_d$  is the Fermi-Dirac distribution.

From this surface conductivity, we can calculate the permittivity of graphene [see Fig. 1.2a].

$$\epsilon_{||}(\omega, \mu_c, \Gamma, T) = \epsilon_r + i \frac{\sigma(\omega, \mu_c, \Gamma, T)}{\epsilon_0 \omega \Delta}, \quad (1.9)$$

where  $\epsilon_r$  is the background relative permittivity and  $\Delta$  is the sheet thickness. The permittivity of graphene is dependent on the doping level

Surface plasmon polaritons, hereafter referred to as plasmons, occur at the interface of a metal and a dielectric. We do not discuss bulk plasmons in this work. Plasmons are a collective oscillation that consists of both light propagating in a dielectric and a coherent oscillation of electrons in the metal. For graphene, these excitations are typically at infrared frequencies and are dependent on the Fermi level of the material [25].

$$\omega_0 \propto E_f^{1/2} \propto n_0^{1/4}, \quad (1.10)$$

where  $\omega_0$  is the plasma frequency of the graphene. The  $n^{1/4}$  of the carrier concentration deviates from that of the usual  $n^{1/2}$  for other 2D electron gases[22]. Graphene plasmons sharply confine light. The confinement of graphene,  $\lambda_0/\lambda_p$ , can reach values of 40-80.

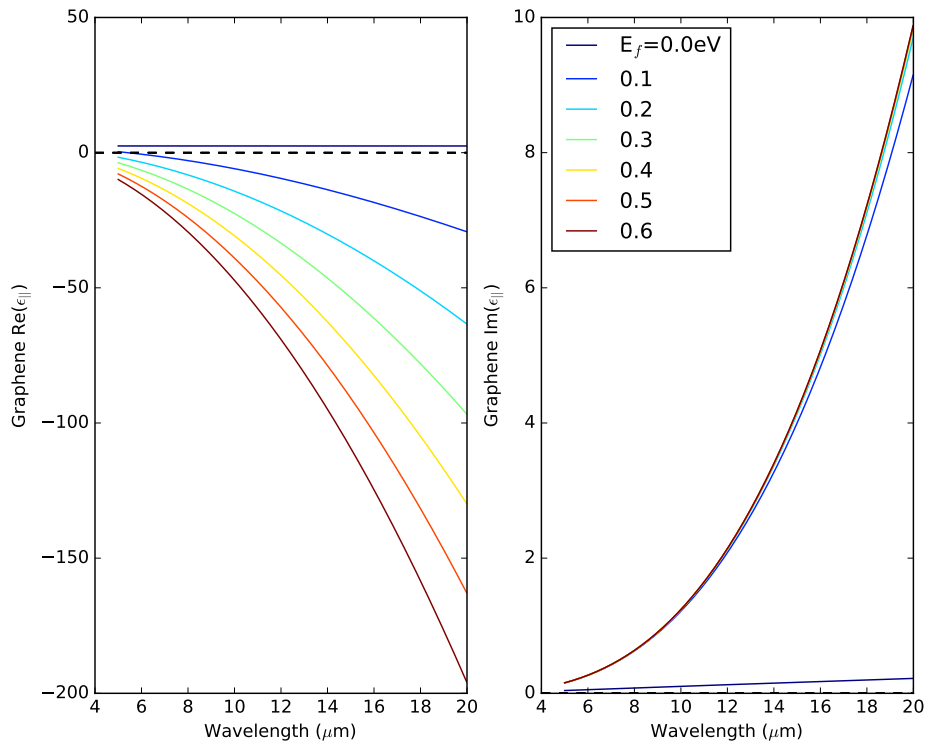


Figure 1.2: The permittivity of the in-plane components of graphene. As the material is doped, the  $\text{Re}(\epsilon)$  goes negative as the graphene acts as a metal. This negative  $\text{Re}(\epsilon)$  enables graphene's plasmonic behavior.

### Spontaneous emission

The control of the spontaneous emission rate of near-field dipole is dependent on the local field of the emitter. Fermi's Golden Rule states [27]

$$\Gamma_{fi} = \frac{2\pi}{\hbar} \left| \langle f, 1_k | H_{int} | i, 0_k \rangle \right|^2 \rho(\hbar\omega_k), \quad (1.11)$$

where  $H_{int} = \boldsymbol{\mu} \cdot \mathbf{E}$  is the interaction Hamiltonian between a dipole and the electric field,  $\rho$  is the photonic density of states, and  $\omega_k = \omega_{fi}$ . It shows the decay of the state  $|i, 0_k\rangle$  into the  $\langle f, 1_k|$  at a rate of  $\gamma_{fi}$ . In case of plasmonics, the interaction of the electric field is greatly enhanced as light is confined to extremely small mode volumes. Additionally, the local density of states is enhanced. These factors contribute to a high Purcell enhancement[28]

$$F_P = (3\lambda_0^3 Q)/(4\pi^2 n^3 V), \quad (1.12)$$

where the resonant wavelength is  $\lambda = \lambda_0/n$ ,  $Q$  is the quality factor, and  $V$  is the mode volume. Purcell enhancement is a figure of merit often considered in cavity

design, as the greater the Purcell enhancement, the greater the coupling between a cavity and an emitter. In the case of graphene, the low mode volume gives  $F_P$  on the order of  $10^6 \sim 10^7$  for graphene ribbons [29].

### 1.3 Hyperbolic metamaterials

#### Metamaterials

Metamaterials are materials composed of subwavelength elements that together make up an effective material. By changing the behavior of these subwavelength elements, one can choose the properties of the material. There are many techniques to describe the effective index of the metamaterial, such as the Maxwell Garnett approximation or effective medium theory. They allow the creation of new effective materials that would be difficult or impossible to find in normal materials.

Metamaterials have broad applications due to their flexibility. As they can use a variety of materials, permittivity and permeability can be engineered based on the thickness of layers for 1D metamaterials, or for arbitrary structures with 3D metamaterials. They have been used for graded index materials [30], cloaking [31, 32], negative index materials, photon-induced transparency [33], and transformation optics [34].

#### Hyperbolicity

The inquiry into hyperbolic materials began with Veselago's concept of a material with a negative refractive index [35]. Hyperbolic materials consist of materials with  $\epsilon$  of different signs with the following dispersion relation:

$$\frac{k_x^2 + k_y^2}{\epsilon_e} + \frac{k_z^2}{\epsilon_o} = \frac{\omega^2}{c^2}. \quad (1.13)$$

This difference creates a hyperbolic dispersion relation. Rather than having a finite sphere of available photonic states, dispersion relation becomes a hyperboloid of infinite size. This divergence in the number of states is limited by the finite size of the unit cell  $k_{max} \sim 1/a$ , leading a  $\rho \sim k_{max}^3$  [36], as well as the size of the emitter  $s$ , as  $F_{Pmax} \sim \lambda_0^3/s^3$ . There is additionally distance dependent coupling between the dipole and the hyperbolic sheet. There is also spatial dispersion in the hydrodynamical Drude model, leading to  $\rho_{max} < \omega^2/v_F^3$  [37]. Despite these limitations, hyperbolic materials have the potential for potentially huge enhancements of the density of states.

Hyperbolic materials have many uses[38, 39], including nano-imaging, subdiffraction lithography, hyperlensing, nanosensing, fluorescence engineering, and control of thermal emission [40]. They allow for broadband enhancement of spontaneous emission rates.

#### **1.4 The Scope of this thesis**

This thesis explores electrically-gated graphene in controlling light emission and propagation.

Chapter 2 focuses on the simulation of graphene nanoribbons near  $\text{Er}^{3+}$  emitters. By electrostatically tuning the graphene carrier concentration, we can change the response of near-field erbium atoms. By modeling  $\text{Er}^{3+}$  as the three level system strongly coupled to plasmons, we can explore the population dynamics and luminescence.

Chapter 3 focuses on the fabrication, measurement, and theory of a graphene/ $\text{SiO}_2$ -based metamaterial stack. By tuning the graphene, we can change in the ordinary and extraordinary response of the material. By changing the behavior at the epsilon-near-zero point, we can obtain hyperbolic dispersion by having permittivities of opposite signs.

Chapter 4 focuses on a graphene/black phosphorus (BP) heterostructure, exploring them with theory and simulation. BP is a 2D hyperbolic material, and by using graphene we can tune the effective response of the heterostructure. This mechanism allows for electrostatic control of hyperbolic behavior, emission of plasmons, and beam angle of emission.

## *Chapter 2*

### ERBIUM LOCAL DENSITY OF STATES MODIFICATION BY GRAPHENE

We propose and theoretically demonstrate electrically tunable photoluminescence from erbium ions ( $\text{Er}^{3+}$ ) coupled to graphene nanoribbons. Through electrostatic tuning of the graphene plasmon, we control the lifetimes of the upper  ${}^4\text{I}_{11/2} \leftrightarrow {}^4\text{I}_{13/2}$  and lower  ${}^4\text{I}_{13/2} \leftrightarrow {}^4\text{I}_{15/2}$  transitions. We show a 28-fold enhancement of doped graphene luminescence at 1535 nm relative to the undoped case. We can tunably induce population inversion on the transition  ${}^4\text{I}_{13/2} \leftrightarrow {}^4\text{I}_{15/2}$ , leading to an overall increase of luminescence by 80% at 1535 nm.

#### 2.1 Introduction

Surface plasmons polaritons (plasmons), the near-field collective oscillation of electron density coupled to electromagnetic waves[41], have generated significant interest due to their subwavelength confinement of light and enhancement of spontaneous emission for near-field resonant particles[42]. [43, 44, 45]. In the presence of a near-field plasmonic cavity, an emitter will preferentially emit into the cavity rather free space due to the high Purcell enhancement of the cavity[46]. Graphene, a known tunable plasmonic material, has been used to modulate spontaneous emission [47, 48]. Plasmonic ribbons can quench fluorescence [49, 50] and have significant propagation losses [51]. These losses pose a significant challenge, and to overcome it various techniques have been applied, often involving introducing a gain medium [52, 53, 54, 55, 56]. As the losses directly relates to the confinement and field enhancement[57], they are a necessary component of strong field enhancement.

Three-level lasers use an optical pump to drive energy the highest excited state [58, 59]. These carriers spontaneously decay to the middle level, whose population controls the light emission from the laser. In these systems, sensitizers can be used to transfer energy from the top level to the  $\text{Er}^{3+}$  [60]. We introduce a novel technique to electrically tunably modulate this energy transfer between the top and middle level by coupling to graphene resonators. This method of controlling lifetimes of multi-level system by using of plasmons opens new possibilities for engineering the light emission of emitters.

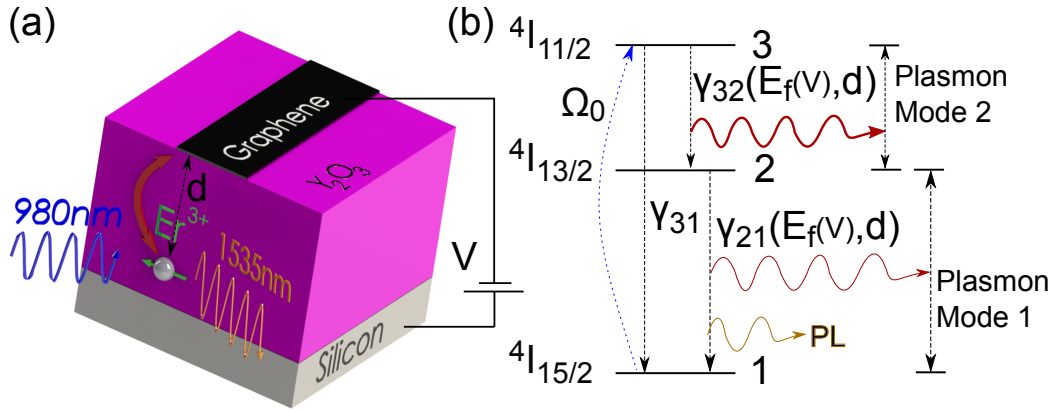


Figure 2.1: (a) An  $\text{Er}^{3+}$  ion in  $\text{Y}_2\text{O}_3$  is excited by a 980 nm laser at distance  $d$  to a 8 nm wide graphene nanoribbon. It emits at  $2.74 \mu\text{m}$  for the  ${}^4I_{11/2} \rightarrow {}^4I_{13/2}$  transition and  $1535 \text{ nm}$  for the  ${}^4I_{13/2} \rightarrow {}^4I_{15/2}$  transition. (b) The three-level system of the  $\text{Er}^{3+}$  couples to two graphene plasmons. The  $\text{Er}^{3+}$  is pumped at  $\Omega_0$ . The  $2.74 \mu\text{m}$  transition occurs at rate  $\gamma_{32}$  and depends on the graphene Fermi level and the distance between the emitter and the graphene ribbon. The  $1.535 \mu\text{m}$  transition occurs at rate  $\gamma_{32}$ .

## 2.2 System Overview: Graphene Ribbons on $\text{Er}^{3+}:\text{Y}_2\text{O}_3$

Our system is a graphene nanoribbon on top of a  $\text{Er}^{3+}:\text{Y}_2\text{O}_3$  [see Fig. 2.1a].  $\text{Er}^{3+}:\text{Y}_2\text{O}_3$  is a known laser material [61, 62]. We treat  $\text{Er}^{3+}$  as a three-level system [see Fig. 2.1b]. The  ${}^4I_{15/2}$  is the ground state  $|1\rangle$ , the  ${}^4I_{13/2}$  the middle state  $|2\rangle$ , and the  ${}^4I_{11/2}$  the top state  $|3\rangle$ . The  $\text{Er}^{3+}$  is pumped at 980 nm. It spontaneously emits at  $2.74(1.535) \mu\text{m}$  with a lifetime of  $4.2\text{ms}(8.8\text{ms})$  in the case of no graphene [63, 64].

An 8 nm graphene ribbon is electrostatically doped via a silicon backgate [see Fig. 2.1a], allowing us to tune the Fermi level of the graphene. The ribbon acts as Fabry-Perot resonator [65]. We use an FDTD simulation to find the behavior of the structure, representing the  $\text{Er}^{3+}$  emission with a dipole source. The dipole is located 1 nm from the edge of the ribbon and a distance  $d$  normal to the plane of the graphene. It excites a high electric field in the surrounding area [see Fig. 2.2] as it couples to the plasmonic modes of the ribbon.

The graphene plasmon modes are broad and Fermi-level dependent. An 8 nm ribbon with Fermi doping of  $0.64\text{eV}$  has a mode between  $2.7 \mu\text{m}$  and  $3.4 \mu\text{m}$ , whereas a 8 nm ribbon with a Fermi doping of  $0 \text{ eV}$  supports a plasmon further out in the IR. When the graphene is tuned on resonance with the erbium emission, the light is more strongly coupled to plasmonic mode. There is also weaker plasmonic coupling

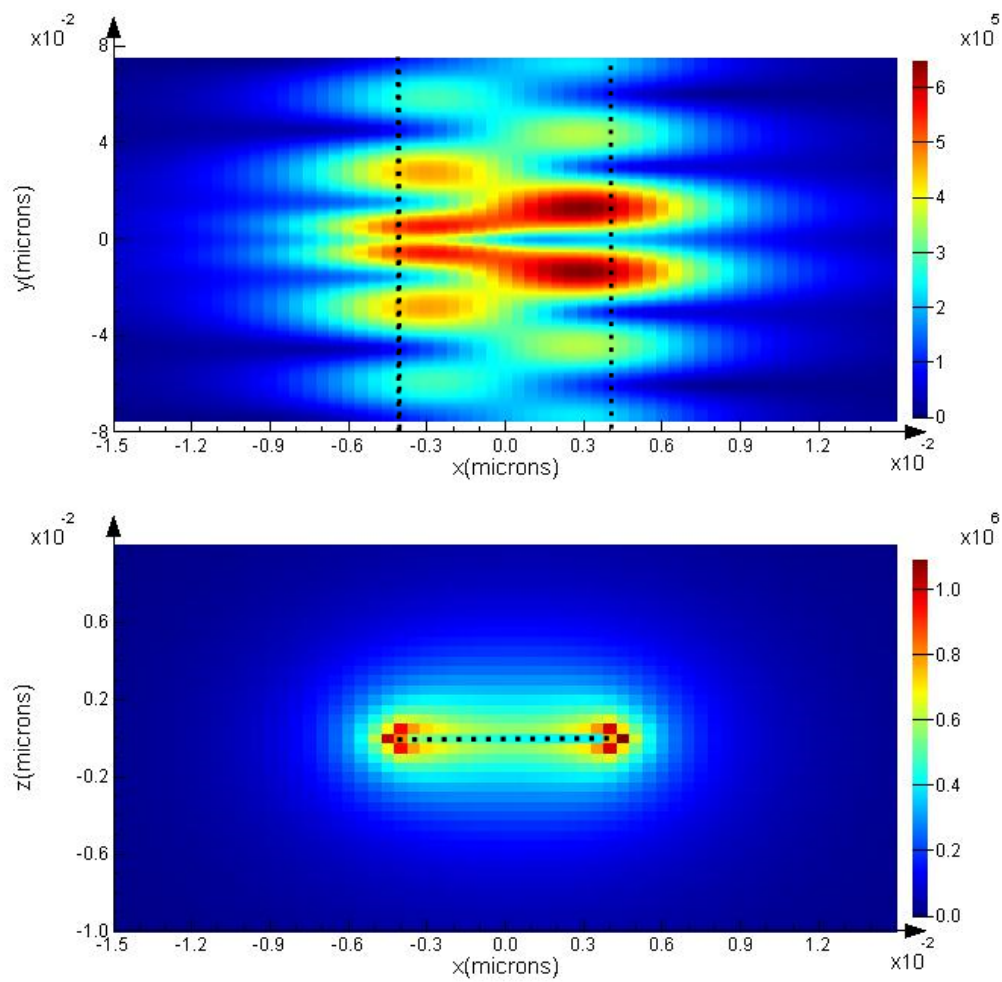


Figure 2.2: The electric field  $|E|$  of the 8 nm graphene nanoribbon. The top perspective is viewed at a height of 20 nm and the side view is at a distance of 20 nm. It is excited by a  $2.74 \mu\text{m}$  dipole 1 nm below the edge of the ribbon and supports plasmon of wavelength  $\lambda_p = \lambda_0/93$ .

at 1535 nm.

The plasmonic coupling changes the local density of states and enhances the electric field, leading to a Purcell enhancement of the spontaneous emission rate according to Fermi's Golden Rule. In order to calculate this change, we used the Green's function approach, allowing us to calculate the spontaneous emission rate  $\gamma$  from the imaginary part of the Green's function  $\mathbf{G}$  at the location of the dipole [66].

$$\gamma = \frac{\pi\omega_0}{3\hbar\epsilon_0} |\mathbf{p}|^2 \rho_p(\mathbf{r}_0, \omega_0) \quad (2.1)$$

$$\rho_p(\mathbf{r}_0, \omega_0) = \frac{6\omega_0}{\pi c^2} \left[ \mathbf{n}_p \cdot \text{Im} \left\{ \overleftrightarrow{\mathbf{G}}(\mathbf{r}_0, \mathbf{r}_0; \omega_0) \right\} \cdot \mathbf{n}_p \right]. \quad (2.2)$$

This change in spontaneous emission rate is affected by the Fermi level of the graphene [see Fig. 2.3]. At 12 nm distance, as we raise the transition Fermi level, there is a decrease in relative transmission rate at 1535 nm. In contrast, for the 2.74  $\mu\text{m}$ , we see a definite decrease at for  $E_f=0.32$  eV and  $E_f=0.48$  eV, then a subsequent increase for  $E_f=0.64$  eV. This shows that close to the plasmon resonance, there's a suppression of the spontaneous emission rate relative to the completely off-resonance case. On resonance, there is a significant increase in transition rate.

We have modeled our three-level gain medium ( $\text{Er}^{3+}$ ) interacting with the graphene nanoribbon plasmon fields on the transitions  $|2\rangle \leftrightarrow |1\rangle$  and  $|3\rangle \leftrightarrow |2\rangle$  using the Liouville-von Neumann equation [67]

$$\dot{\rho} = -\frac{i}{\hbar} [H, \rho^{(i)}] - \mathcal{L}\rho^{(j)}, \quad (2.3)$$

where  $\mathcal{L}$  is the Lindblad superoperator which quantifies the dissipative part of the master equation, the superscript  $j$  denotes the  $j^{\text{th}}$  gain medium  $\text{Er}^{3+}$  ion. The interaction Hamiltonian  $H$ , in rotating wave approximation, can be written as

$$H = \hbar \left\{ \sum_j \left[ -\Delta_1^{(j)} |1\rangle\langle 1| + \Delta_2^{(j)} |3\rangle\langle 3| - \left( \Omega_1^{(j)} |2\rangle\langle 1| + \Omega_2^{(j)} |3\rangle\langle 2| + \Omega_0 |3\rangle\langle 1| + \text{H.c.} \right) \right] \right\}. \quad (2.4)$$

Here the detunings  $\Delta_{1,2} = \omega_{1,2} - \nu_{1,2}$  where  $\omega_{1,2}$  is the atomic transition frequency corresponding to the transition  $|2\rangle \leftrightarrow |1\rangle$  and  $|3\rangle \leftrightarrow |2\rangle$  respectively. The frequency of the graphene nanoribbon plasmonic mode coupled to the transitions  $|2\rangle \leftrightarrow |1\rangle$  and  $|3\rangle \leftrightarrow |2\rangle$  are  $\nu_{1,2}$  respectively. The emitter density of matrix elements  $\rho_{ij}$  of

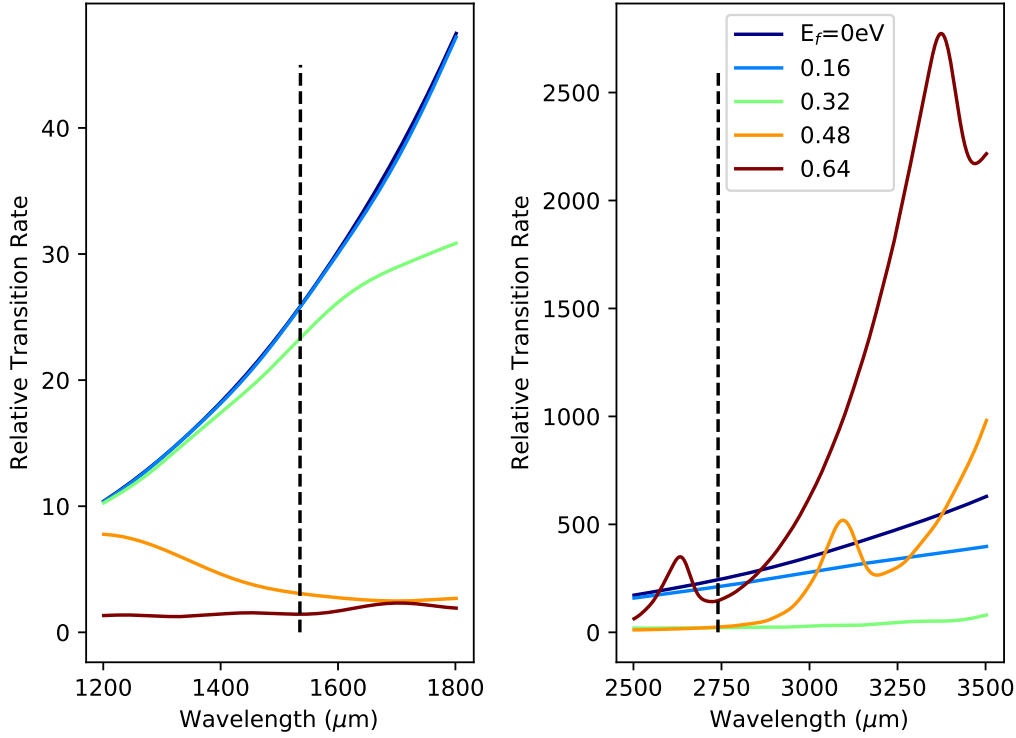


Figure 2.3: The relative transition rates for two different on-resonance ribbon widths for a dipole 12 nm from a 8 nm graphene ribbon. By modulating the Fermi level, we can control the transition rate at  $2.74 \mu\text{m}$  as well as at  $1535 \text{ nm}$ . The black dashed lines indicate the transitions of the  $\text{Er}^{3+}:\text{Y}_2\text{O}_3$ . The transition rate is relative to that of a dipole not next to graphene.

the  $j^{\text{th}}$  gain medium Erbium ion is given by the coupled partial differential equation as follows:

$$\dot{\rho}_{11} = \gamma_{21}\rho_{22} + \gamma_{31}\rho_{33} + i(\Omega_0^*\rho_{31} - \Omega_0\rho_{31}^*) + i(\Omega_1^*\rho_{21} - \Omega_1\rho_{21}^*), \quad (2.5)$$

$$\dot{\rho}_{33} = (\gamma_{31} + \gamma_{32})\rho_{33} - i(\Omega_0^*\rho_{31} - \Omega_0\rho_{31}^*) - i(\Omega_2^*\rho_{32} - \Omega_2\rho_{32}^*), \quad (2.6)$$

$$\dot{\rho}_{21} = -(\Gamma_{21} + i\Delta_1)\rho_{21} - i\Omega_1(\rho_{22} - \rho_{11}) + i\Omega_2^*\rho_{31} - i\Omega_0\rho_{32}^*, \quad (2.7)$$

$$\dot{\rho}_{31} = -(\Gamma_{31} + i\Delta_1 + i\Delta_2)\rho_{31} - i\Omega_0(\rho_{33} - \rho_{11}) - i\Omega_1\rho_{32} + i\Omega_2\rho_{21}, \quad (2.8)$$

$$\dot{\rho}_{32} = -(\Gamma_{32} + i\Delta_2)\rho_{32} - i\Omega_2(\rho_{33} - \rho_{22}) - i\Omega_1^*\rho_{31} + i\Omega_0\rho_{21}^*, \quad (2.9)$$

$$\rho_{11} + \rho_{22} + \rho_{33} = 1, \quad (2.10)$$

where the relaxation rates are  $\Gamma_{21} = \frac{1}{2}\gamma_{21} + \gamma_{ph}$ ,  $\Gamma_{31} = \frac{1}{2}(\gamma_{31} + \gamma_{32}) + \gamma_{ph} + i(\Delta_2 + \Delta_1)$ , and  $\Gamma_{32} = \frac{1}{2}(\gamma_{31} + \gamma_{21} + \gamma_{32}) + \gamma_{ph}$ . The Rabi frequency is defined as  $\Omega_1 = \mathcal{E}_1\varphi_{21}/2\hbar$  and  $\Omega_2 = \mathcal{E}_2\varphi_{32}/2\hbar$ , where  $\varphi_{21}$  and  $\varphi_{32}$  are the dipole moments corresponding the

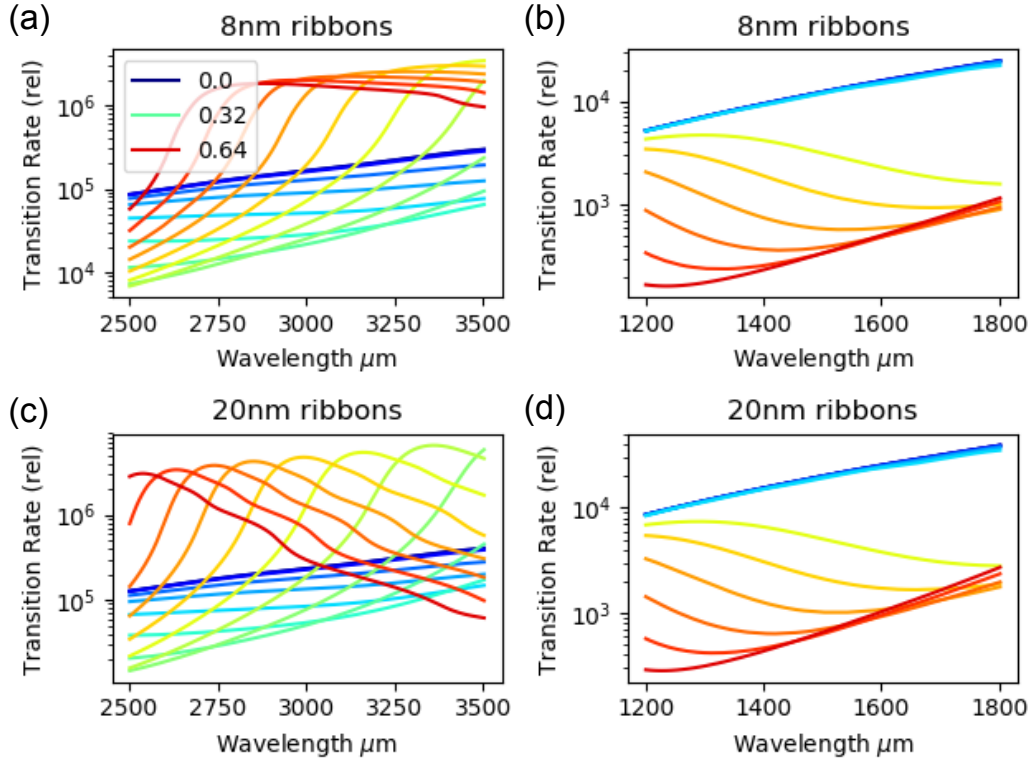


Figure 2.4: The radiative emission rate of a dipole position 1 nm above the metamaterial relative to a dipole with no graphene. The graphene Fermi level is varied to tune the relative couple of (a,b) 8 nm ribbons and (c,d) 20 nm graphene ribbons. (a,c) Plasmons near the  ${}^4I_{11/2} \rightarrow {}^4I_{13/2}$  transition. (b,d) Plasmons near the  ${}^4I_{13/2} \rightarrow {}^4I_{15/2}$  transition.

transitions  $|2\rangle \leftrightarrow |1\rangle$  and  $|3\rangle \leftrightarrow |2\rangle$ . Here,  $\gamma_{ij}$  are the decay rates for populations and  $\gamma_{ph}$  is the phase relaxation (or dephasing) rate of the coherence  $\rho_{ij}$  due to coupling with phonons, surface defects, etc.[68]. The emission of plasmons is described by the coherent polarization of the gain medium corresponding to the transition  $|2\rangle \rightarrow |1\rangle$  and  $|3\rangle \rightarrow |2\rangle$  respectively. The corresponding time evolution equation is obtained using the Heisenberg equation of motion for the amplitudes  $a_{1,2}$  and adding the SP relaxation rate  $\gamma_{1,2}$  respectively. Here  $|a_{1,2}|^2$  quantifies the number of plasmon generated by the emission on transitions  $|2\rangle \leftrightarrow |1\rangle$  and  $|3\rangle \leftrightarrow |2\rangle$ . It has a similar form to the equation for the two-level gain medium, since the same transition is coupled to the plasmon field:

$$\dot{a}_1 = -\Gamma_1 a_1 + i \sum_j \rho_{21}^{(j)} \tilde{\Omega}_1^{(j)}, \quad (2.11)$$

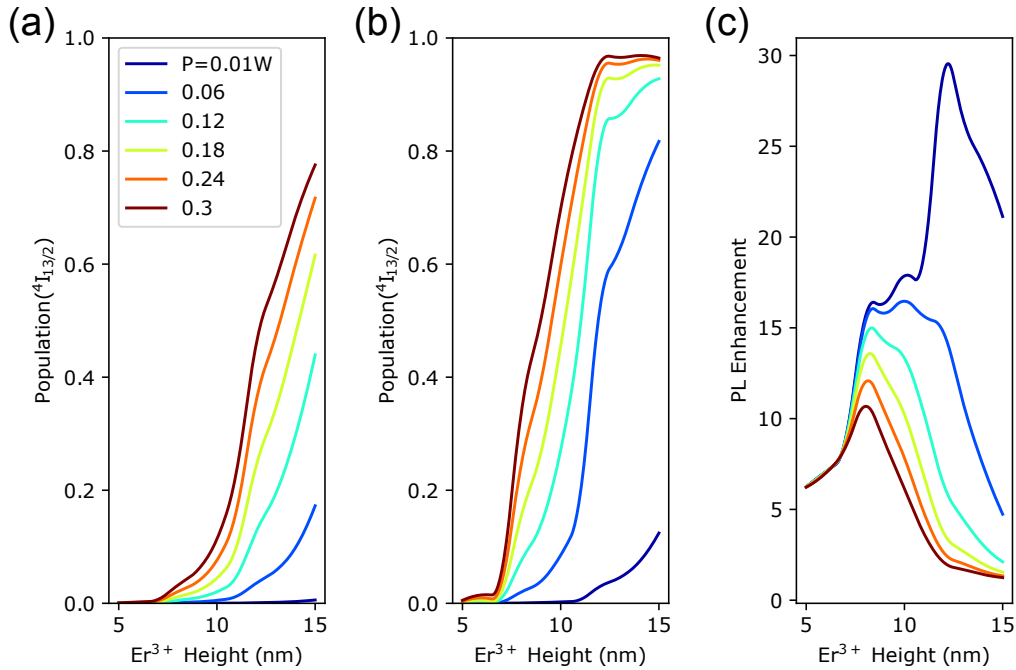


Figure 2.5: The population of the  ${}^4I_{13/2}$  level is dependent on distance and the graphene Fermi level. The PL enhancement is the ratio of the graphene at  $E_f=0.64$  eV to  $E_f=0.0$  eV. By optimizing the distance to 12 nm, we can attain a high PL enhancement of 28 with pump powers under 10mW.

$$\dot{a}_2 = -\Gamma_2 a_2 + i \sum_j \rho_{32}^{(j)} \tilde{\Omega}_2^{(j)}, \quad (2.12)$$

where  $\Gamma_1 = \gamma_1 + i\Delta_n$ ,  $\tilde{\Omega}_1^{(p)} = \mathcal{E}_1 \rho_{21} / 2\hbar = \Omega_1^{(p)} / a_1$  similarly  $\tilde{\Omega}_2^{(p)} = \mathcal{E}_2 \rho_{32} / 2\hbar = \Omega_2^{(p)} / a_2$  is a single plasmon Rabi frequency.

### 2.3 Results and discussion: Enhancement of Luminescence

From the rate equations, we can compute the overall occupation of the luminescent  ${}^4I_{13/2} \rightarrow {}^4I_{15/2}$  transition based on distance, pump power, and Fermi level. We first consider the effects of distance on luminescence [see Fig. 2.5]. Emitters that are close to the graphene ribbon are significantly suppressed. As the emitter moves farther away, there's an increase in luminescence and, at 8 nm, the  $E_f=0.64$  eV case shows an increase of luminescence compared erbium without graphene. The luminescence ratio of PL( $E_f=0.64$  eV) to PL( $E_f=0$  eV) is a maximum of 28-fold enhancement at 12 nm for powers under 10mW. The PL ratio achieves maximum at this distance due to the saturation in the underlying rates. The population will saturate to unity with sufficient distance for the PL( $E_f=0.64$  eV) and there is a

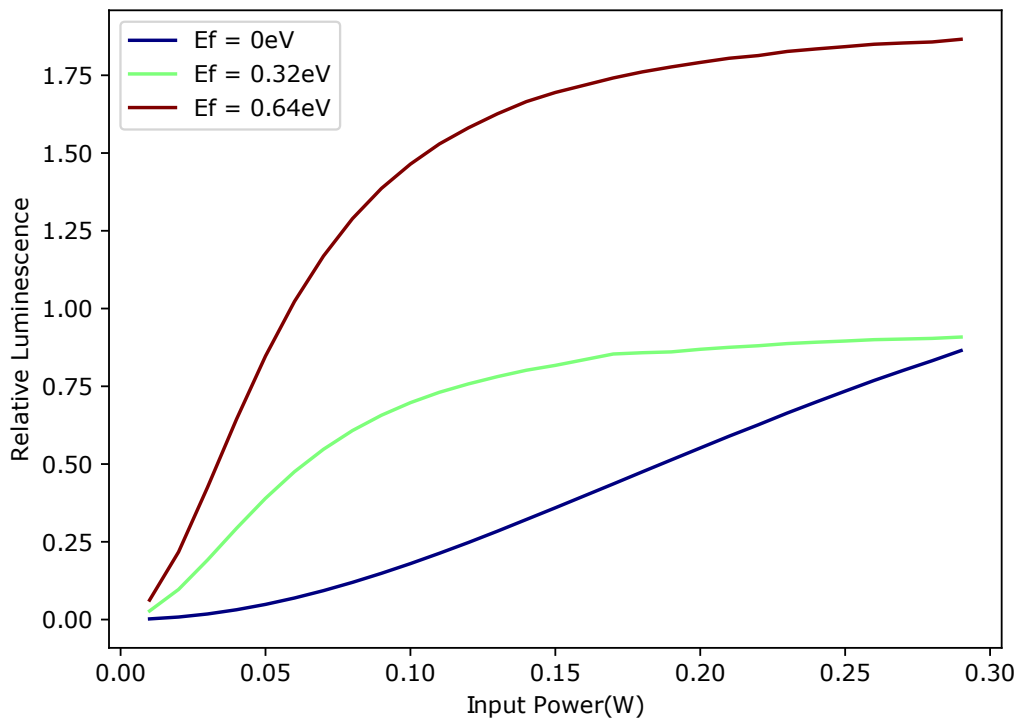


Figure 2.6: Steady-state luminescence  $\text{Er}^{3+}$  ions coupled to on and off resonance graphene nanoribbons relative to  $\text{Er}^{3+}$  emission with no graphene. Doping greatly increases the luminescence of  $\text{Er}^{3+}$  relative from the  $E_f=0$  to  $E_f=0.64$  eV. Above 50mW, we show an overall increase in luminescence for heavily doped graphene. Beyond 300mW, we hit the optical damage threshold[69]

steady increase of the  $\text{PL}(E_f=0 \text{ eV})$  with distance. This maximum luminescence modulation depth of 14dB occurs at 12 nm.

If we look at a fixed distance across different input powers and Fermi levels, as in Fig. 2.5, we can see a clear increase in luminescence with applied bias. With over 5mW of power, we see an increase in relative luminescence compared to the emission without graphene. By applying a graphene gate, we can induce population inversion in  $\text{Er}^{3+}$ . The upper transition is enhanced by orders of magnitude whereas the lower transition has near unity enhancement, so the  ${}^4I_{13/2}$  state becomes more heavily occupied. Whereas in the no-graphene case, the lifetime of the levels were roughly equal, with graphene we can introduce a huge enhancement to the upper transition while only slightly perturbing the lower transition rate.

Another interesting consequence the rate increases is that the rates attain their steady state populations over an order of magnitude more quickly [see Fig. 2.7] than the

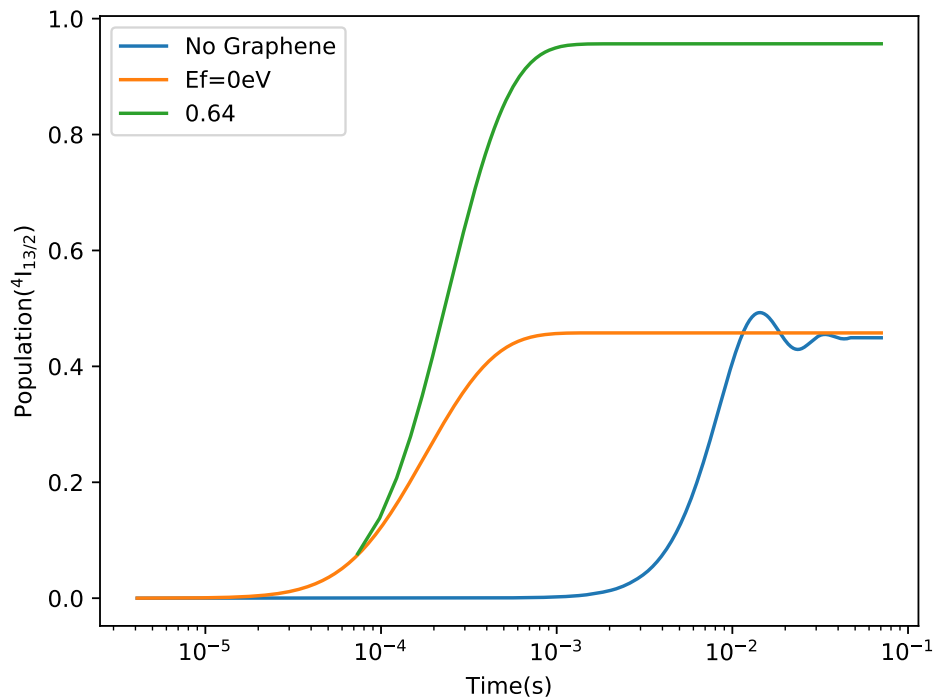


Figure 2.7: Graphene nanoribbons more rapidly enhance the luminescence as they fill the  ${}^4I_{13/2}$  state sooner than normal erbium. We assume an incident power of 0.3W.

no graphene case. As we enhance the speed of various transition rates, the system should attain steady state more quickly. If the dipole were closer to the erbium, we would see an even quicker rise time, but the overall luminescence would decrease.

## 2.4 Conclusions

We can electrostatically control the photoluminescence of  $\text{Er}^{3+}$  through tunable plasmonic coupling to a graphene nanoribbon. When the erbium ion is within 5 nm of the ribbon, the transition rates are plasmonically enhanced, quenching emission as the electrons rapidly return to the ground state. As the erbium is moved away from the ribbon, the coupling strength decreases. At sufficient distance, we see a net increase in luminescence, as the spontaneous emission rate from the top level is significantly enhanced, leading to a greater occupation of the middle state. At low pump powers, we show a 28-fold enhancement of photoluminescence of the doped graphene as compared to the undoped case. At high pump powers, we can attain population inversion of the middle state, leading to a 1.8-fold enhancement of

luminescence compared to erbium without graphene. Additionally, this inversion is electrostatically tunable, and can be turned on and suppressed with electrostatic doping of graphene. This effect occurs an order of magnitude more quickly than transitions in uncoupled  $\text{Er}^{3+}$ .

Tunable plasmonic control of electronic transition rates in multi-level systems presents a novel method for control over the carrier dynamics of systems. This technique could be applied to lasers, LEDs, and other electronic systems. Although plasmons are often thought of as only being sources of quenching in luminescent systems, this approach demonstrates a way that they can be used to tunably increase luminescence instead of quenching it. Plasmons provide a novel and electrically tunable mechanism for controlling the lifetime of emitters.

## EXPERIMENTAL DEMONSTRATION OF TUNABLE GRAPHENE HYPERBOLIC METAMATERIAL

Previous theoretical work has suggested that actively tunable graphene elements can enable the tuning of the dielectric permittivity of metamaterials through the permittivity near zero (ENZ) regime at infrared wavelengths to yield transition from an elliptical to hyperbolic dispersion. Here, we experimentally realize and measure the response of a graphene/polar dielectric metamaterial using a graphene-SiO<sub>2</sub> unit cell. This metamaterial exhibits epsilon-near-zero crossing and tunable electric properties from  $E_f=0$  to  $E_f=0.5$  eV that are experimentally verified through spectroscopic ellipsometry and transmission measurements.

### 3.1 Introduction

Metamaterials are artificial composite materials with subwavelength elements that exhibit electromagnetic responses unseen in the natural world. Research in the field has been mainly driven by the desire to tailor the optical response of materials [70, 71, 36]. Particularly interesting is the case of a permittivity ( $\epsilon$ ) near zero (ENZ) [72, 73, 74], for which one can design materials with a high photonic density of states such as hyperbolic or indefinite metamaterials (HMMs). These are typically composed as uniaxial metamaterials whose ordinary, in-plane ( $\epsilon_o$ ) and extraordinary, out-of-plane ( $\epsilon_e$ ) electrical permittivities have opposite signs.

$$\frac{k_x^2 + k_y^2}{\epsilon_e} + \frac{k_z^2}{\epsilon_o} = \frac{\omega^2}{c^2}. \quad (3.1)$$

This peculiar dielectric response creates a hyperbolic dispersion relation, allowing for open isofrequency surfaces and a continuum of wavevectors extending to large values for a given energy. Owing to these novel optical properties, hyperbolic metamaterials can exhibit large Purcell factor enhancements and can serve as slow-light media [75], enhance dipole-dipole interactions [76], and increase gain in lasing [55], as well as enable super-resolution [77] or sub-diffraction imaging [78].

Graphene is a well-studied monolayer material for electronics [79] and infrared photonics [80] and holds promise for active metamaterials [81]. Specifically, the

dielectric properties of graphene can be dynamically tuned by chemical or electrostatic modulation of the carrier concentration [82], allowing the design of graphene-dielectric layered metamaterials [83, 84, 85]. Additionally, it has been shown theoretically and experimentally that the plasmonic nature of graphene supports surface electromagnetic waves with extreme confinement [22, 29]. This field localization, together with the tunability of graphene, provides a promising platform for investigating tunable graphene-based HMMs. There has been considerable theoretic effort in the past decade to understand the properties of tunable graphene metamaterials. [86, 87, 88, 89, 85, 90, 84, 91]. Graphene-based HMMs can further enhance the already strong field localization of graphene plasmons due to the opposing signs of dielectric permittivity along the different coordinate axes. Graphene heterostructures have been proposed for applications including thermophotovoltaics [92], tunable absorbers [86], thermal and terahertz emission [93, 84], device applications [94], photonic logic switches [95], and elliptic-hyperbolic transitions [85]. Experimental demonstrations of graphene metamaterials utilized chemically doped graphene in order to fix metamaterial behavior [96].

### 3.2 Fabrication Challenges

While graphene metamaterials have been widely explored in theoretical work, fabrication challenges have hampered experimental realization of promising structures. As a two-dimensional material with weak out-of-plane Van der Waals forces, graphene exhibits poor adhesion to most dielectric substrates. Moreover, it has been challenging to fabricate methods for dielectric over-layers on graphene that are sufficiently large in area to enable metamaterial characterization and which also avoid oxidization or other damage to the graphene structure. We overcome these challenges and experimentally demonstrate a planar graphene-SiO<sub>2</sub> metamaterial, which is electrically gate-tunable with an external bias. A thin Al<sub>2</sub>O<sub>3</sub> layer encapsulates the graphene and enables adhesion of the top SiO<sub>2</sub> to realize symmetric dielectric heterostructures. This structure exhibits a tunable optical response in the long wavelength infrared range. We predict the tunable dielectric properties of our metamaterial and compare these predictions to experimental results obtained from spectroscopic ellipsometry and reflectometry, yielding the first experimental demonstration of a graphene metamaterial with a tunable uniaxial near-zero permittivity.

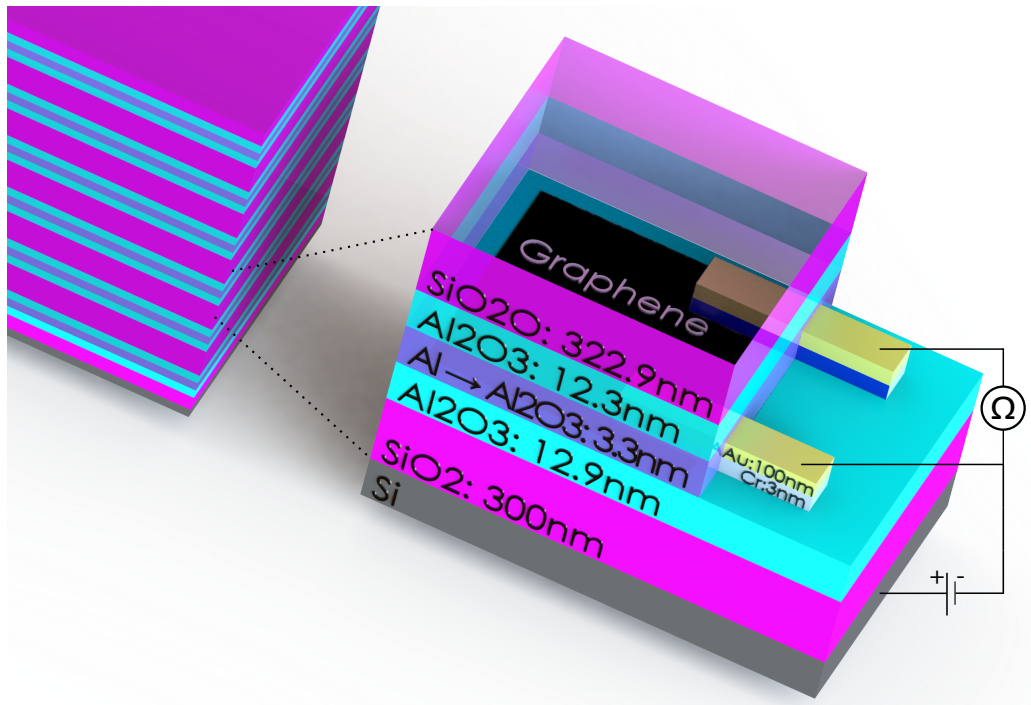


Figure 3.1: Left: Schematic of a theoretical metamaterial stack. Right: Schematic of the fabricated individual device. The layers: Lightly-doped silicon substrate, thermally-grown SiO<sub>2</sub>, atomic layer deposited (ALD) Al<sub>2</sub>O<sub>3</sub>, transferred chemical-vapor deposited (CVD) graphene, electron-beam evaporated Al, ALD Al<sub>2</sub>O<sub>3</sub>, and plasma-enhance chemical vapor deposition SiO<sub>2</sub>. The thin layers of Al<sub>2</sub>O<sub>3</sub> are necessary for feasibility fabrication. The thick SiO<sub>2</sub> contribute to the majority of the dielectric response. Contacts are added to gate and measure the resistance of the graphene. The graphene is tuned by gating against the back silicon substrate.

### 3.3 SiO<sub>2</sub>/Al<sub>2</sub>O<sub>3</sub>/Graphene Heterostructure

We consider a metamaterial where monolayer graphene is sandwiched between two polar dielectric materials as depicted in Fig. 3.1. Observations show an  $\epsilon$  near-zero response between the polar dielectric resonances of the dielectric, in contrast to previous proposals which assumed non-dispersive materials between graphene sheets [83]. The dielectric material has two phonons, and the real part of  $\epsilon$  spans from positive to negative values, therefore crossing zero. By electrostatically tuning the graphene carrier density and permittivity, we can shift the point at which the real part of the in-plane permittivity ( $\text{Re}(\epsilon_o)$ ) crosses zero. Since the graphene response is uniaxial, we can shift the  $\text{Re}(\epsilon_o)$  while leaving the extraordinary ENZ point unchanged.

The electrical modulation of permittivity occurs in the plane of the graphene sheet,

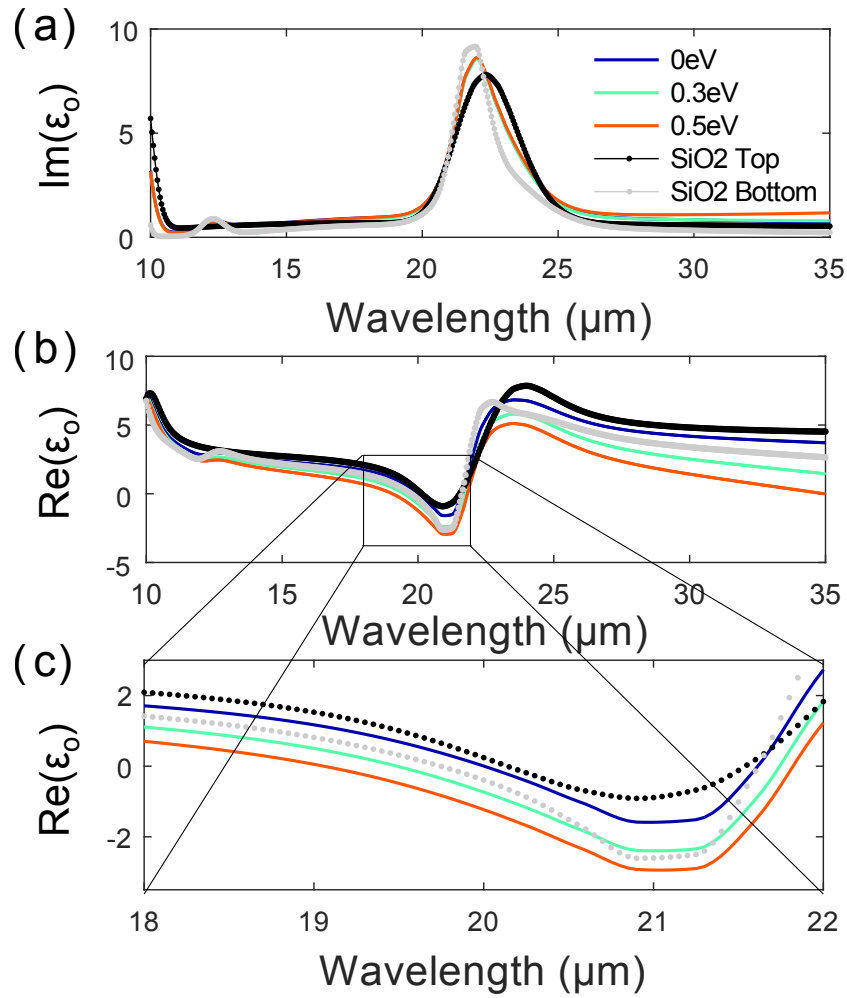


Figure 3.2: Material parameter retrieval is used on the ellipsometric data for SiO<sub>2</sub> and graphene to calculate effective  $\epsilon_o$  that is tuned with an electrical bias over a range of Fermi levels from 0 to 0.5 eV. (a) Imaginary value of  $\epsilon_o$  for the SiO<sub>2</sub> and overall structure. (b) Real part of  $\epsilon_o$ . (c) Inset where the real part of  $\epsilon_o$  crosses zero at a range of wavelengths depending on the  $E_f$ .

and thus should largely affect  $\epsilon_o$ . Out of plane, the graphene has a constant  $\epsilon_o$ . The effective permittivity of the homogenized structure should consist of a tunable  $\text{Re}(\epsilon_o)$  that crosses zero at a range of wavelengths for different Fermi level values and a static out-of-plane permittivity ( $\epsilon_e$ ) that crosses zero at a fixed wavelength.

The metamaterial has been designed to function experimentally with a tunable  $\epsilon$  with the desired performance. The substrate is a lightly-doped silicon wafer, with a 300 nm thick layer of thermal oxide. On top of that oxide, we deposit 12.9 nm of  $\text{Al}_2\text{O}_3$  by atomic layer deposition (ALD). CVD-grown graphene is transferred onto the stack. A 0.5 nm aluminum layer is deposited on top of the graphene by electron-beam evaporation and oxidizes in ambient conditions. Another layer of 12.3 nm  $\text{Al}_2\text{O}_3$  is deposited on top of the stack. The final layer is deposited by plasma-enhanced chemical vapor deposition (PECVD) and consists of 321 nm of  $\text{SiO}_2$ . Lithographically-defined patterns were used to deposit 3 nm/100 nm of Cr/Au contacts on the graphene layer. These contacts were used to gate the graphene against the silicon backgate. This allows for the electrical tuning of the effective  $\epsilon_o$  of the metamaterial. The effective Fermi level was calculated using a capacitor model based on the materials between the gate and the applied voltage[97].

$$E_f = 0.031\sqrt{V - V_{Dirac}}. \quad (3.2)$$

The location of the Dirac peak was experimentally determined using a capacitor model and the measured change in resistance. The thickness of the film layers was measured by both a thin film analyzer and visible ellipsometry with a qualitative agreement of roughly 2 nm.

The previous absence of experimental demonstrations of graphene/dielectric tunable hyperbolic response can be attributed to several factors: first, large-area graphene sheets on the order of  $\text{mm}^2$ 's with gate-induced tunability are needed to perform metamaterial optical measurements. Exfoliated flakes are generally limited to sizes of 10s of  $\mu\text{m}$ , so large-area graphene samples grown by chemical vapor deposition and subsequently transferred from their growth substrates are necessary. Second, deposition of large-area thin dielectric layers on graphene is challenging. Films prepared by electron-beam evaporation exhibit thermal stress-induced delamination [98]. . Films grown by atomic layer deposition (ALD) with an  $\text{H}_2\text{O}$  precursors exhibit difficulty in bonding to chemically-inert hydrophobic graphene [99], whereas ozone-based ALD processes oxidize the graphene sheet. A viable dielectric deposition method was developed consisting of functionalization of the surface by

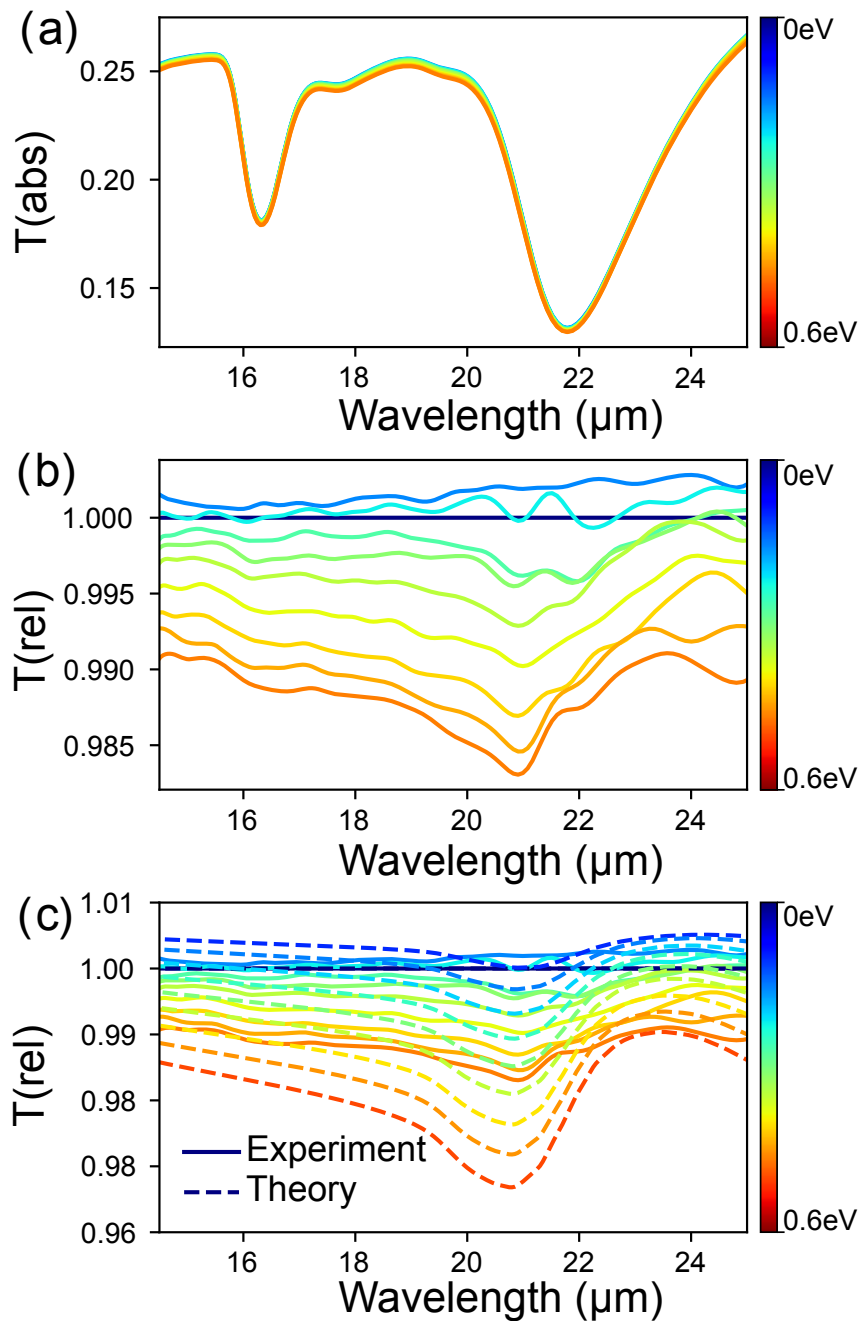


Figure 3.3: (a) Absolute FTIR transmission over a range of Fermi levels. (b) Experimental data normalized to  $E_f=0$  eV, the Dirac point. (c) Experiment compared with theory, based on ellipsometric fits of the thickness and optical properties constituent layers. Normalized to  $E_f=0$  eV. Deviations arise due to hysteresis of the graphene induced by charge trapping.

deposition of trimethylaluminium (TMA) [100] or an aluminum nucleation layer [101] to create a seed layer for additional deposition. A suitably thin layer of aluminum is needed so that it can fully oxidize and not compromise the electrical gating of the graphene. In order to create a symmetric metamaterial unit cell, ALD  $\text{Al}_2\text{O}_3$  layers need to be deposited. We found that deposition of  $\text{Al}_2\text{O}_3$  via plasma-enhanced chemical vapor deposition (PECVD) resulted in reduced thermal stress and avoided delamination.

### 3.4 Effective permittivity via transfer matrices and parameter retrieval

Metamaterial structures comprised of alternating layers of polar dielectric materials and graphene have two key characteristics. First, polar dielectric materials exhibit Reststrahlen bands of negative dielectric permittivity across the infrared range, which allow the near-zero crossing of the effective dielectric response of the heterostructure. Second, polar dielectric materials have high electrical breakdown strengths that support the high applied electric fields. They allow for high contrast in the optical response of graphene. We use the Kubo formula [102] calculate the sheet conductance  $\sigma$  from the  $E_f$  of graphene. This value can be used to compute the transfer matrix for graphene [103].

$$\overleftrightarrow{G} = \begin{bmatrix} 1 & 0 \\ 4\pi\sigma/c & 0 \end{bmatrix}$$

We utilize the transfer matrix approach [104], accounting for graphene via  $G$ , and obtain the complex scattering amplitudes of the fields. In turn, we use these to compute the effective permittivity via previously developed parameter retrieval approaches [105]. We measure individual layers of our sample with ellipsometry to obtain the ellipsometric parameters ( $\psi$ ,  $\Delta$ ). Using oscillator models for the constituent materials, we transform  $\psi$  and  $\Delta$  into a complex  $\epsilon$  using conventional ellipsometric fitting. From these values, we can calculate transfer matrices of the dielectric layers. Combining these with the graphene transfer function, we obtain the transfer function of the effective medium [104]. This function gives us the complex scattering amplitudes of the fields for the structure. Using material parameter retrieval [105], we can solve the inverse problem to compute effective  $\epsilon_o$  [see Fig. 3.2(a,b)] and  $\epsilon_e$  for a range of graphene Fermi levels.

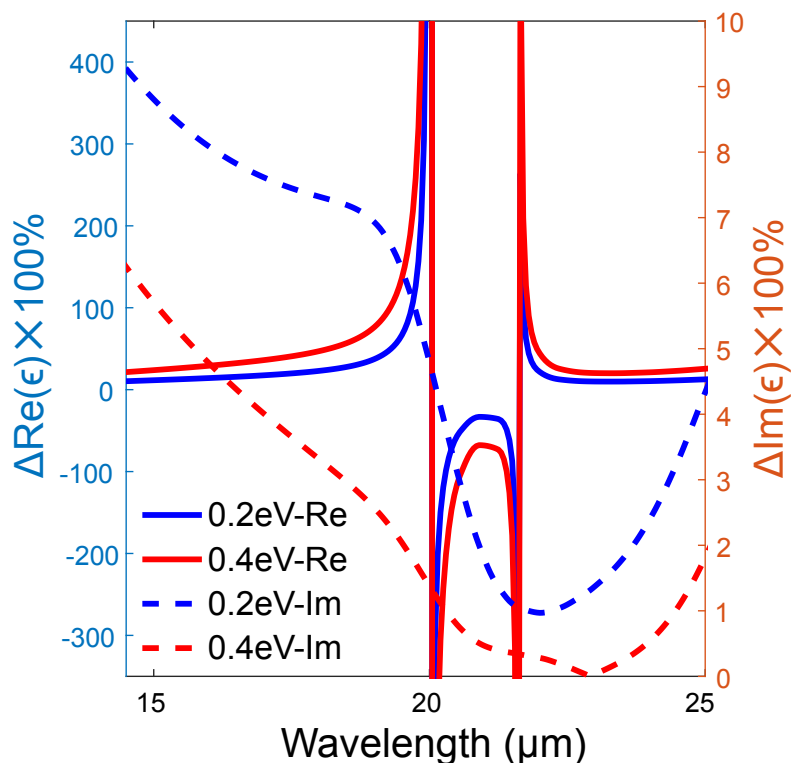


Figure 3.4: Change of  $\epsilon$  with applied bias.

### 3.5 FITR Measurements of tunable permittivity

Fourier-transform infrared spectroscopy (FTIR) was used to measure sample transmission and compare with predictions for  $\epsilon$  calculated by material parameter retrieval. By tuning the graphene, we were able to induce a change in transmission [See Fig. 3.3]. Our calculations predicted the experimentally-observed direction for ENZ wavelength shift. Graphene becomes more metallic at higher carrier concentration, thereby increasing in absorption. This shift of the graphene Drude conductivity causes modulation of the effective permittivity of the metamaterial. The graphene exhibits hysteresis, which is attributed to defects induced by deposition of the Al layer, which may account for the discrepancies between experiment and theory. As the graphene is tuned, the Dirac peak shifts in the direction of applied bias, causing the sample to experience a reduced  $E_f$ , giving qualitative experimental agreement with theory without fitting parameters.

By tuning  $\epsilon$ , we have interesting behavior that occurs at the ENZ points near the  $\text{SiO}_2$  phonon at  $22.0 \mu\text{m}$  [see Fig. 3.2(c)]. The out-of-plane  $\epsilon_e$  extraordinary crossing is at  $19.7 \mu\text{m}$  and  $21.1 \mu\text{m}$ , whereas the in-plane ordinary crossing occurs at a broader

range of wavelengths dependent on the Fermi level of the graphene. From the  $19.7 \mu\text{m}$  ENZ point to  $20.0 \mu\text{m}$ ,  $\text{Re}(\epsilon_o)$  is greater than zero for  $E_f=0 \text{ eV}$ , whereas  $\text{Re}(\epsilon_e)$  is negative. This implies our heterostructure should behave as Type I hyperbolic metamaterial (HMM). As the graphene Fermi level is raised to  $0.2 \text{ eV}$ , this region shrinks. Above  $E_f=0.2 \text{ eV}$ , the  $\text{Re}(\epsilon_o)<0$  while  $\text{Re}(\epsilon_e)>0$ , as expected for a type II HMM. At  $0.5 \text{ eV}$ , this phenomenon occurs in the wavelength range from  $19.1 \mu\text{m}$  to  $19.7 \mu\text{m}$ . This observation is consistent with an electrically tunable elliptic-to-hyperbolic transition in metamaterial dispersion for both type I and type II HMMs. For the longer wavelength crossings, the material should behave as a type I HMM for wavelengths in the range between  $21.1 \mu\text{m}$  and  $21.6 \mu\text{m}$  for  $E_f = 0 \text{ eV}$  and up to  $21.8 \mu\text{m}$  for  $E_f = 0.5 \text{ eV}$ .

### 3.6 Conclusions

In summary, we have experimentally demonstrated a graphene metamaterial with tunable epsilon-near-zero permittivity response. By tuning the graphene Fermi level, we can modulate the ENZ wavelength by up to  $0.9 \mu\text{m}$ . Ellipsometry was used to determine the optical properties of the constituent materials. Material parameter retrieval was used to calculate the constitutive electromagnetic response. These calculations closely matched the FTIR transmission measurements of the overall heterostructure, indicating a shift of the graphene permittivity near the ENZ point under electrical gate bias. Near  $19.7 \mu\text{m}$  we can tune electrically tune  $\epsilon$ , which implies an elliptical to hyperbolic transition in dispersion.

### 3.7 Methods: Fabrication

In this section, we will describe the process used to fabricate the metamaterial. The device required extensive process engineering. Of the nine different layers in the heterostructure, many methods were employed in order to find the optimal process. In addition, several other device geometries were explored. The initial conception of the project was more a simple  $\text{SiO}_2/\text{Graphene}/\text{SiO}_2$ . This original concept was expanded greatly in order to make a device that was symmetric, large area, and stable in air.

The substrate was purchased from MTI. It was a  $300\text{nm}$  thermally grown  $\text{SiO}_2$  on Si. The silicon was P-type B-doped and  $0.5\text{mm}$  thick, and had a (100) crystal orientation and with an R of  $1\text{-}10 \Omega\text{cm}$ .

Material	Thickness (nm) Filmetric	Thickness (nm) Visible Ellipsometry	Process
SiO <sub>2</sub>	321.77	322.93	PECVD
Al <sub>2</sub> O <sub>3</sub>	12.92	12.3	ALD 135 Cycles
Al→Al <sub>2</sub> O <sub>3</sub>	4.63	3.27	E-beam
Graphene			Transferred
Al <sub>2</sub> O <sub>3</sub>	10.41	12.88	ALD 150 cycles
SiO <sub>2</sub>	301.18	300.46	MTI: Thermal
Si			MTI Bought

Figure 3.5: A layer by layer depiction of the full graphene metamaterial stack, the layer thickness by two different modes of measurement, and the process used to create the layer.

#### Atomic layer deposition of Al<sub>2</sub>O<sub>3</sub>

Deposition of the Al<sub>2</sub>O<sub>3</sub> was performed using a Fiji G2 Plasma Enhanced Atomic Layer Deposition System. TMA was used as the precursor. The chamber was heated to 150°C. This layer allowed for a greater gate bias to be applied, as Al<sub>2</sub>O<sub>3</sub> has a high breakdown strength. Additionally, application of a thin layer of Al<sub>2</sub>O<sub>3</sub> would fill pin-holes in the underlying material, which are the sources of failure in graphene gate bias measurements.

#### Graphene Transfer

The graphene on copper with PMMA was purchased from Graphena and had a specification sheet mobility of  $3,760 \frac{cm^2}{Vs}$ . Raman measurements were used to confirm that the graphene was primarily monolayer [see Fig. 3.10a]. Graphene transfer allows the graphene to be moved from the copper to the SiO<sub>2</sub>/Si substrate. The PMMA-graphene-copper sheet is cut to size, and then placed into a dish of ferric chloride. After approximately eight minutes, the copper is fully eaten away.

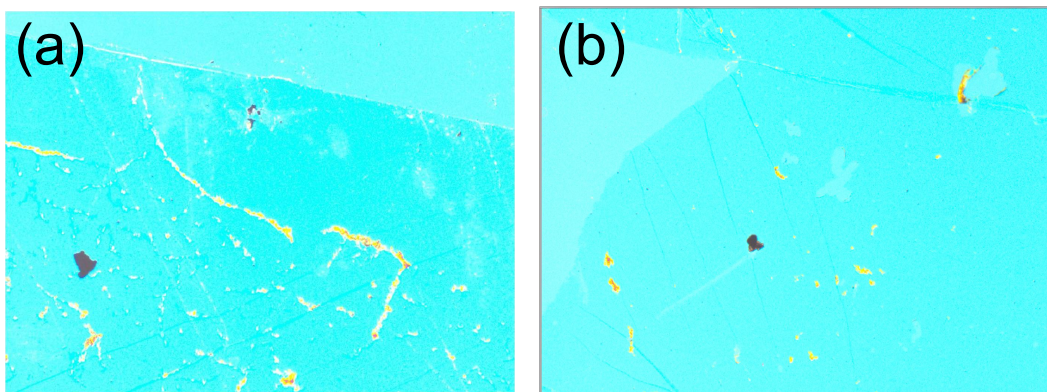


Figure 3.6: An image of PMMA on graphene using a confocal microscope. (a) The graphene had been immersed in acetone for 45 minutes, but this did not remove all the PMMA, as shown by the orange patches. (b) The graphene with three acetone baths of 45 minutes

The remaining PMMA/graphene sheet is scooped up with a spoon and placed in a succession of four water baths. Care must be taken in order to pick up the floating sheet without having it stick to the sides. Spraying water breaks the surface tension of the water, allowing for an easier transfer. Large baths, coupled with wait times, allow the samples to be fully cleaned of iron chloride. Immediately before the transfer, the SiO<sub>2</sub>/Si substrates are cleaned in an oxygen plasma clean. This process makes the sample more hydrophobic, allowing the graphene to more readily stick to the surface. The SiO<sub>2</sub>/Si chip is used to scoop the graphene out of the final water bath. It is then heated overnight at 60°C in order to evaporate the water that was caught between the graphene sheet and the substrate.

### **PMMA removal from graphene**

Initially, 45 minutes in acetone was used to remove PMMA [see Fig. 3.6a]. However, this immersion did not fully remove the residue. PG remover was not a solution, as it resulted in the complete removal of the graphene.

The final procedure consisted of the sample being placed in a succession of three acetone baths at 60°C for 45 minutes. Between each step, the sample is thoroughly rinsed with acetone for 15 seconds before being placed in a new bath of fresh acetone. Care must be taken for the graphene never to be exposed directly to air, as the acetone will evaporate and destroy the graphene. For the final cleaning steps, it is placed in a beaker of isopropanol, taken out and sprayed with isopropanol, and finally sprayed with compressed nitrogen. This process did not fully remove the PMMA, but did

remove significantly more PMMA than just 45 minutes in acetone[see Fig. 3.6b].

### **Cr/Au Contacts**

Contacts are initially patterned using a Raith 5000+ direct write electron beam (e-beam) lithography system. A two layer resist is used. The first layer consists of PMMA 495A4 deposited at 3000rpm for 60 seconds and baked at 180C for 150 seconds. The second layer consists of PMMA 950A2 deposited at 3000rpm for 60 seconds and baked at 180C for 150 seconds. A two-layer resist was used in order to have a cleaner lift-off process. The lower molecular weight resist dissolves first, allowing the top to be removed. Single layer resists can stick to the sample, making it difficult to remove the metallization layer.

The contacts are deposited using a CHA Mark 40 e-beam evaporator. The contacts are 3 nm of Cr deposited at 0.5 Å/s followed by 100 nm of Au, deposited at 1.5 Å/s. These contacts are consistent with those found in literature for gating graphene devices. Once the contacts have been deposited, the e-beam resist is removed by immersing the sample in acetone for 45 minutes. It is then sprayed with acetone to remove any excess gold. It is then sprayed with isopropanol and dried with compressed nitrogen.

### **Aluminum deposition by electron-beam evaporation**

Aluminum was deposited using a Lesker Labline e-beam evaporator. The settings were set to deposit 5 Å at 0.5 Å/s. As the deposition occurred over a relatively short amount of time and a very thin layer of aluminum was deposited, more material would be deposited than was set on the system. Measurement by thin-reflectometry showed a layer thickness of 4.63 nm. Note that the thickness of this layer is important, as it needs to completely oxidize in air in order not to adversely affect the graphene tunability. If the system were set for 10 Å, the electrical properties of the device would be compromised.

This Al was deposited in order to serve as nucleation layer to the follow ALD steps. By adhering metallic Al to the graphene, we can overcome the weak Van Der Waals interaction that precludes adhesion to other materials. Exposure to oxygen naturally oxidizes the Al into Al<sub>2</sub>O<sub>3</sub> in ambient conditions. By depositing a sufficiently thin layer, the native oxide layer penetrates through the entire material. As the carrier concentration of metallic Al is higher than that of semiconducting graphene, a thin metallic layer would sharply change the properties of the resistance measurements of the graphene Dirac peak.

$\text{Al}_2\text{O}_3$  was used over other methods such as 3,4,9,10-perylene tetracarboxylic acid (PTCA) functionalization [106] as it deposits a clean uniform layer. PTCA suffers similar issues to the PMMA removal from the Graphena graphene in that it leaves a non-uniform residue on the sample. As a large area of graphene is needed for the following measurements, the PTCA method was not a viable option.

### **Further atomic layer deposition of $\text{Al}_2\text{O}_3$**

Deposition of the  $\text{Al}_2\text{O}_3$  was again performed using a Fiji G2 Plasma Enhanced Atomic Layer Deposition System. By depositing onto  $\text{Al}_2\text{O}_3$  rather than graphene, the  $\text{Al}_2\text{O}_3$  was able to successfully adhere to the sample. A non-ozone process was used, as ozone would oxidize the graphene[see Fig. 3.10c]. By measuring the thickness of the underlying  $\text{Al}_2\text{O}_3$  layer as well as the Al layer, the number of cycles to be run can be calculated. By reducing the number of layers, we can preserve the symmetry of the structure by ensuring an equal thickness of  $\text{Al}_2\text{O}_3$  above and below the graphene.

### **Plasma-enhanced chemical vapor deposition of $\text{SiO}_2$**

An Oxford PECVD deposits a layer of  $\text{SiO}_2$  on the sample. As PECVD is not a precise process between runs occurring at different times, a number of calibration runs were needed in order to deposit with precision. A PECVD flows gas into a chamber, which then will react and deposit material. Rather than a self-passivating ALD, PECVD deposition rate is dependent on the gas flow over the surface of the chip. Therefore, the deposition is non-uniform, with the edges of the chip receiving less  $\text{SiO}_2$ . This non-uniformity imposes the condition on the experimental design that the chip needs to be sufficiently large that the deposition on the graphene is uniform. By placing a Si chip on the contacts, they can be shielded from the  $\text{SiO}_2$ , which is necessary for the subsequent wire bonding. This requirement also imposes the condition that the contact pads need to be sufficiently long. A shielding Si chip is placed sufficiently far away, typically a few mm's, such that the deposition on the graphene remains relatively uniform.

The reason PECVD was selected over other methods to deposit the top  $\text{SiO}_2$  is that it does not induce lamination. Other methods of deposition, such as electron-beam evaporation will delaminate [see Fig. 3.7]. PECVD was run at 200 °C, a lower temperature than is usual with this type of process. The Al nucleation layer does increase the strength of the bond to the graphene of the underlying layer. However, care must be taken to not cause undue stress on the material. Of the available

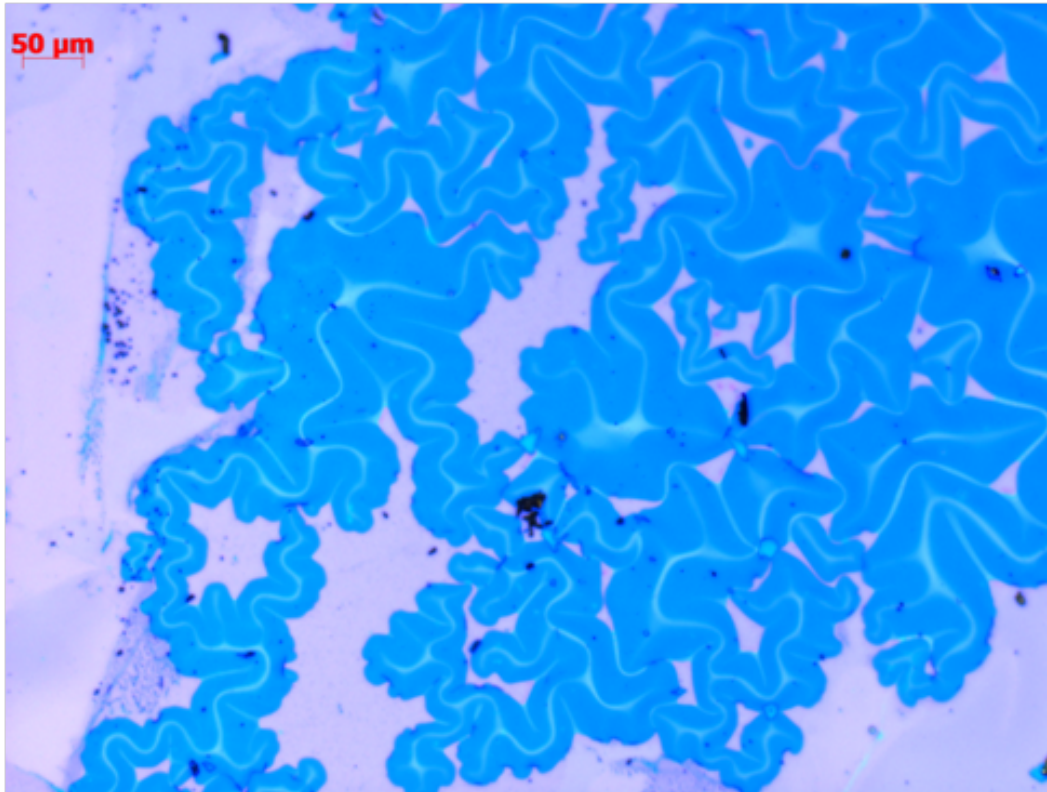


Figure 3.7: Top SiO<sub>2</sub> delaminates from samples when deposited by e-beam evaporation. There is high thermal stress in a film deposited by e-beam evaporation. As the film cools, it causes stress in the film. The effects are visible to the naked eye. Graphene is the pale purple region and occupies most of the area save for the far left region. The blue wave lines are the delaminated regions. The delaminated region covers nearly the entire sheet of graphene. Delamination begins at a single point and spreads across the sample. It can occur a number of minutes after the device has left the e-beam chamber. If the device is left in the e-beam chamber in vacuum to slowly cool overnight, it will still delaminate.

processes, PECVD caused the least thermal stress, leading to it being chosen to deposit the top SiO<sub>2</sub>.

### **Wire Bonding to the contacts**

The contacts need to be bonded to a gold ceramic package in order for there to be proper electrical connections. In addition, the sample needs to have an area of SiO<sub>2</sub> scraped away in order to expose the underlying silicon. This is then cleaned with compressed nitrogen. A wedge-wedge wire bonder westbond model 7476D-79 is used to bond gold wires between the sample contacts and the pads. It uses ultrasonic energy in order to adhere the gold to the pad.

Different amounts of energy needed to be used for different wire bonding steps. A low current was needed for bonding to the gold pads on the ceramic chip. Lower energies were used to bond to the sample itself. The field needed to be sufficient to go through the 12 nm of  $\text{Al}_2\text{O}_3$  and bond to the gold without punching through the material and shorting to the underlying Si. In bonding to the Si directly for the backgate, high fields were used as it is difficult to directly bond gold to Si.

### **Electrical bias**

Electrical biases were applied between the top gold contact and the underlying silicon backgate. The electrical resistance was read using a multimeter between two of the gold contact pads. A bias was applied using a Keithley Sourcemeeter.

The quality of the gate was monitored by recording the leakage current through the  $\text{SiO}_2$ . With little to no bias, the leakage current was under 1 nA [see Fig. 3.8]. As the current was applied. At high voltage levels, a successful gate had under  $1\mu\text{A}$  of current. For samples whose gate failed, the leakage current exceeded  $10\mu\text{A}$  under 2V of bias. If a sample was over-biased, it would fail catastrophically and destroy the sample. The silicon would short to the graphene and high charge would flow across the short. Even after the voltage was reduced, this short would still exist, making the sample unsuitable for gating.

## **3.8 Methods: Sample Characterization**

### **Thickness**

The first method used to measure thickness used a Filmetrics F40 Reflectometer. By knowing the reflectivity of the sample, along with a database of material properties, the Filmetrics calculate the reflectance of the sample. Reference measurements were made on a 704.5 nm of  $\text{SiO}_2$  on Si to verify the machine was working properly and to correct for any drift in accuracy. The fit on all samples was greater than 0.9. Each sample was measured five times at three different positions and results were averaged, then corrected against the reference sample. The standard deviation on thickness was 1 nm or less. The second set of measurements made used a visible ellipsometer. Each sample was measured. A model of the materials were used to fit  $\psi$  and  $\delta$ , which resulted in a thickness. The thicknesses measured by the reflectometer and ellipsometer were in close agreement and only deviated by a few nanometers at most.

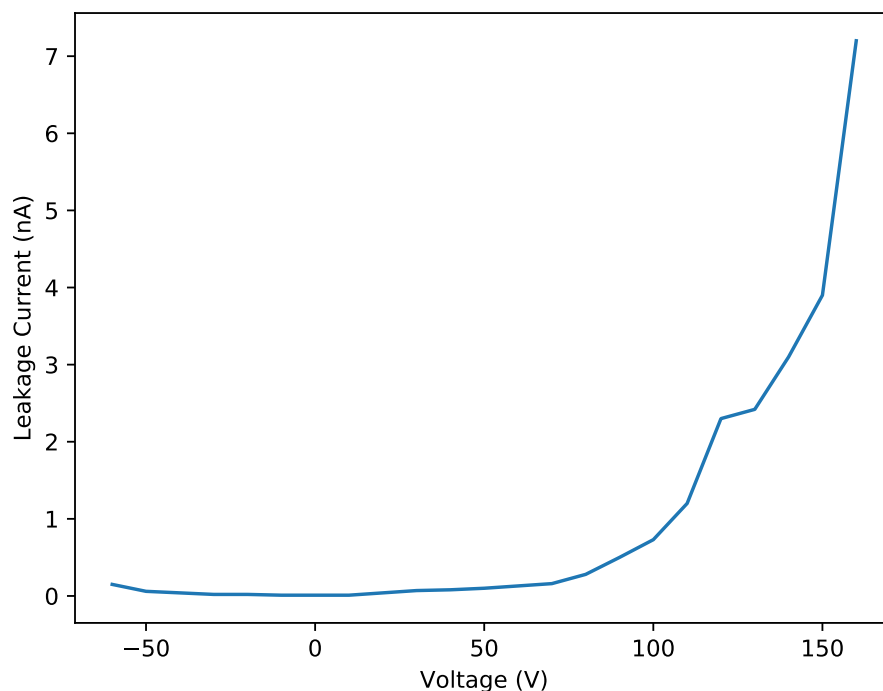


Figure 3.8: A representative response of a sample under going electrical bias. Most samples were tested between -150V and 150V as they were liable to fail much beyond those voltage. There is a sharp increase in the leakage current under high bias.

### Electrical Measurements

Electrical measurements are used to determine the Fermi level of graphene. Initial measurements showed the Dirac Peak occurred at high bias voltages. [see Fig. 3.9a]. However, once a metalization layer of aluminum was deposited on the graphene, there was a large shift in the Fermi level [see Fig. 3.9b]. This effect is theorized to occur due to charge trapping in the graphene. The aluminum oxidizes to  $\text{Al}_2\text{O}_3$ , causing a shift in the Fermi level. There is also a large hysteresis, and when a voltage is applied, the graphene resistance will slowly change with time.

### Raman Measurements

Raman measurements were conducted using a Renishaw M1000 Micro Raman Spectrometer System with a 100 mW 532 nm laser. These measurements [see Fig. 3.10ab] provided confirmation that the graphene was monolayer and that it was not damaged during the fabrication process. These results confirm that the Al

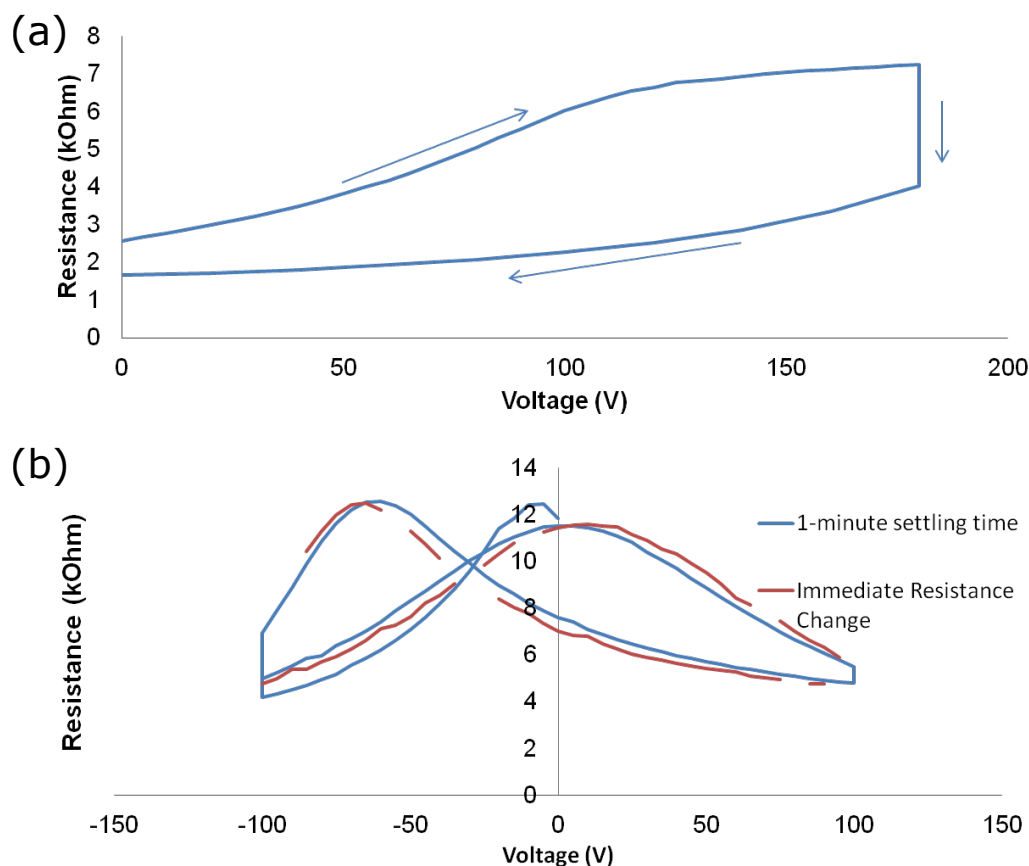


Figure 3.9: (a) Applied bias versus graphene resistance after the graphene was transferred but before ALD. Note that the maximum resistance, the Dirac Peak, is at 180V. (b) Applied bias versus graphene resistance after aluminum metalization. The Dirac peak changes, from -60 V to 0 V due to hysteresis. The two lines represent the resistance measurement that was achieved immediately once hitting the voltage and after a minute of dwell time. Measurements were taken by moving 5 V once a minute and having a 5 minute dwell time at the maximum and minimum voltages.

nucleation layer on top of the graphene successfully protects it from the additional ALD deposition and PECVD. Had it been oxidized, it would have the additional graphene oxide peak as seen in Fig. 3.10c.

### FTIR measurements

The FTIR measurements were conducted using a Thermo-Nicolet iS50 FTIR, courtesy of George Rossman. Measurements were conducted using a variety of detectors and beam splitters in order to encompass a broader range of measurements. For 2-15  $\mu\text{m}$  KBr beam splitter and KBr detector were used. Beyond 15  $\mu\text{m}$ , a far IR polyethylene detector with a KBr beamsplitter was used.

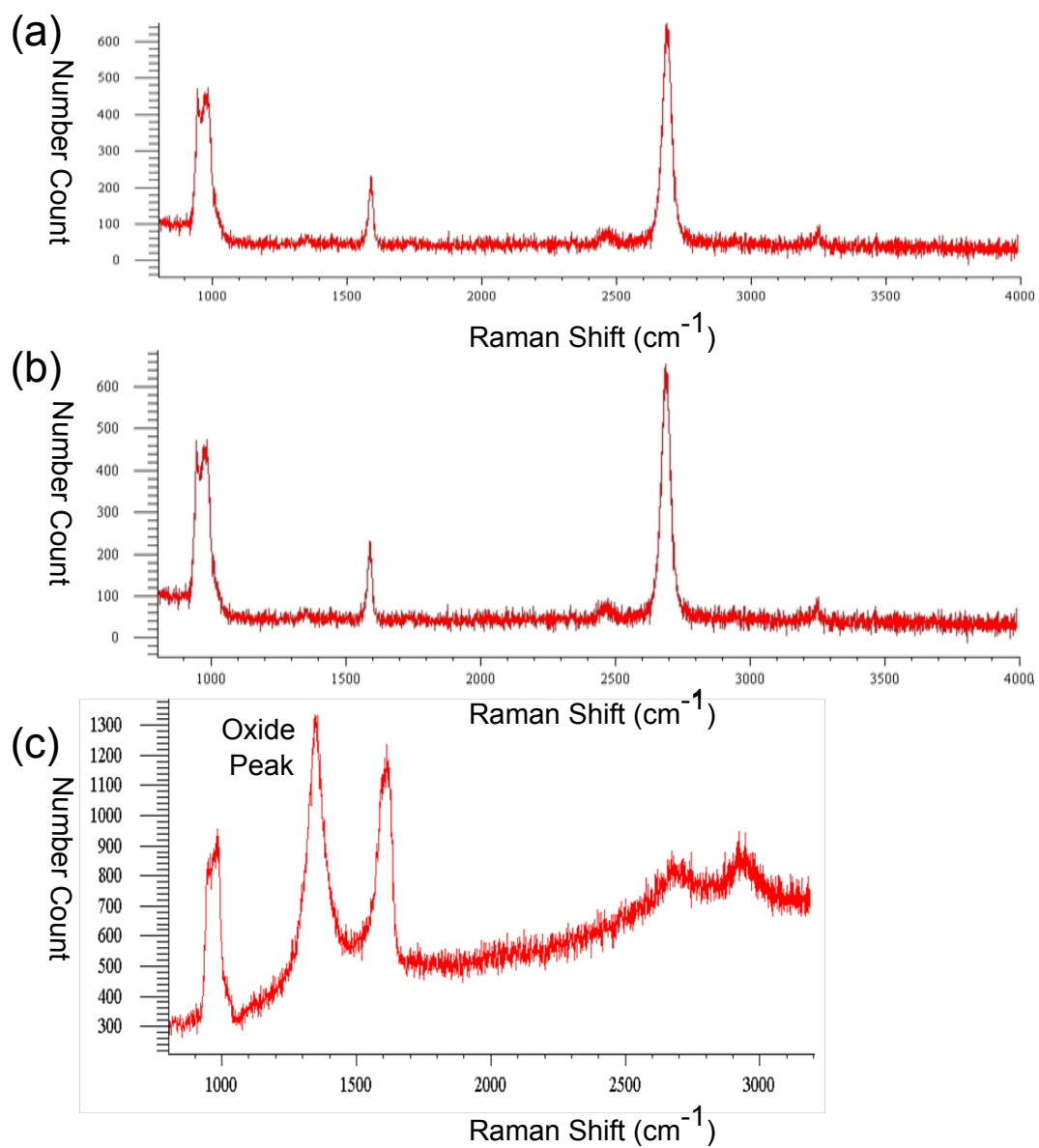


Figure 3.10: (a) Graphene before PECVD (b) Graphene after PECVD. (c) Graphene after ozone-based ALD, an alternative approach not used in making the final sample. The additional peak indicates the presence of graphene oxide.

The measurements were conducted in the main chamber of the FTIR. An adjacent microscope provided the source, but due to the detector configuration, the measurements had to be done in the main chamber with no aligning optics. Therefore, a metal disk with a hole in it was used to select the area of the sample of measurement. The hole was a few mm in diameter. In order to conduct these experiments, it was necessary to visually align the whole with the area of graphene or reference sample. Large area samples of graphene, up to 8 mm by 10 mm, were used in order for this technique to only hit the sample.

In order to calibrate the measurements, a variety of reference measurements were made. Each detector and beam splitter configuration needed separate backgrounds. Additionally, backgrounds taken against the metamaterial without graphene were taken as well. In the post-processing of the data, the sample data was divided by the reference background in order to calculate transmission.

There were a number of sources of noise in the measurement. The sample itself changes the optics of the measurement. As light needs to be transmitted through the thick SiO<sub>2</sub> and underlying silicon in order to reach the detector, it will slightly change the focus of the FTIR. Therefore the ratio of the sample measurements to the reference measurements without the sample were not an absolute measurement. Water vapor contributes noise in the infrared, as water has a number of strong absorption lines. The chamber had a vent system that would gradually purge the water and fill the chamber with nitrogen, reducing the noise from the water vapor. An additional source of noise is detector drift. Over the course of minutes and hours, the detector response will slowly drift. This drift sets a limit on the accuracy of the measurement. By increasing the length of the measurement sampling, the noise drops as the  $\sqrt{n}$ , where n is the sampling time.

### **IR Ellipsometry**

The ellipsometer measurements were conducted using an Woolam IR-Vase ellipsometer. The sample was mounted on a glass slide with carbon tape, then the ellipsometer was aligned and calibrated. Measurements were taken at a 45 degree fixed polarization, a resolution of 16, a bandwidth of 0  $\mu\text{m}$ , 1 cycle, 15 spectra, 100 scans, across a variety of angles ranging from 35 to 75 degrees. In order for this measurement to work, large areas of graphene needed to be used, as the beam size was a few mm across. A technique that was developed but not used in the final measurements was the use of a white paper with a hole in it to act as a mask and

block unwanted reflections.

A set of reference samples were used. By using a reference sample, we could confirm the properties of the substrate, check thickness, and have a basis for the final model. The reference samples that were used were bare silicon, Si with 150 cycles of ALD  $\text{Al}_2\text{O}_3$ , Si with 150 cycles of ALD  $\text{Al}_2\text{O}_3$ , and PECVD  $\text{SiO}_2$ .

The underlying silicon was represented by a general oscillator. We then used a surface roughness layer of 1.36 nm thickness with a 50% fill fraction and a top native oxide layer of 1.635 nm. The thermal  $\text{SiO}_2$  was fitted 295.451 nm, in close agreement with the 300 nm thickness specification of the company we had purchased it from. We had an MSE of 2.612 for the the ellipsometric fit[see Fig. 3.11]. The bottom ALD  $\text{Al}_2\text{O}_3$  layer was 12.8 nm. On top of it was a layer of graphene, represented by a 2 nm thick general IR oscillator. The top Al to  $\text{Al}_2\text{O}_3$  layer was fit as a different material than the ALD layers, as it was deposited by a different method and therefore could have different optical properties. It was 3.72 nm thick. On top of the was 11.85 nm of ALD  $\text{Al}_2\text{O}_3$ . Finally, the PECVD layer was 321 nm thick.

The ellipsometric behavior of the device as a whole was measured [see Fig. 3.12]. It was measured at both the Dirac point and the maximum doping show the greatest tunability of the structure. The measurement was very noisy, in part due to the complex underlying stack. Additionally, the back reflection of the underlying silicon caused partial decoherence of the transmitted polarized light, injecting additional noise into the measurement.

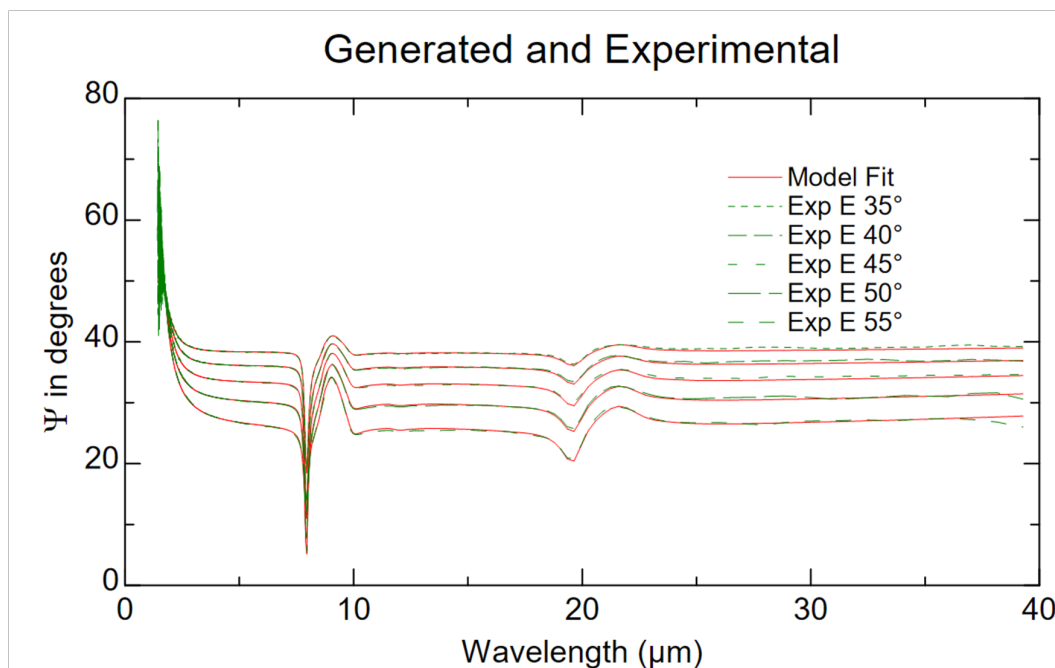


Figure 3.11: The ellipsometer fit of the ellipsometric model to the data for Si/SiO<sub>2</sub>. We see good agreement with the data. There are clear absorption lines of the SiO<sub>2</sub> near 8nm and 20nm due to phonons.

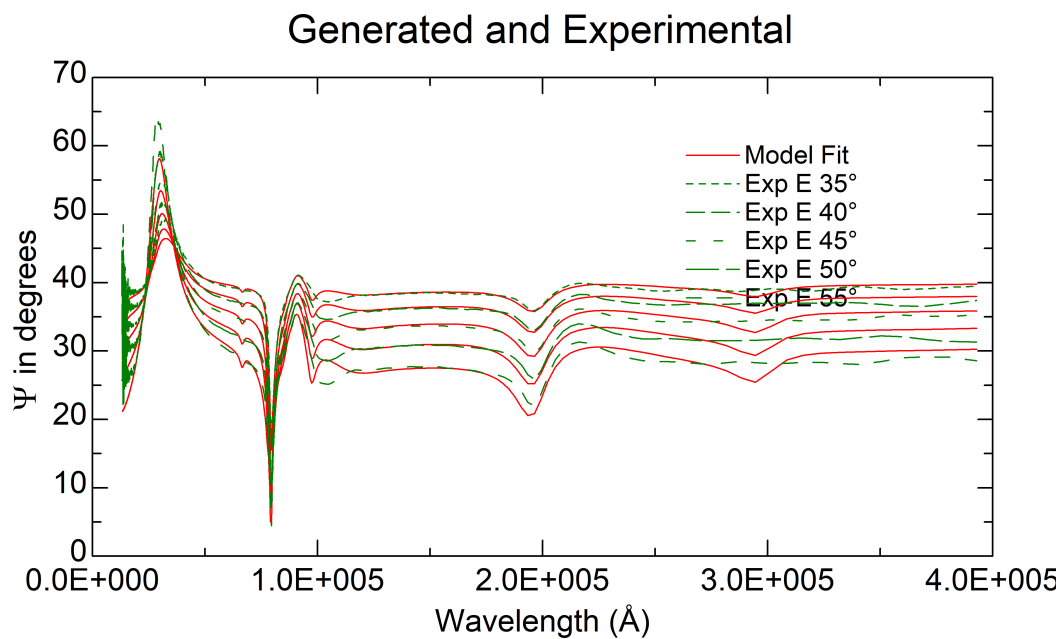


Figure 3.12: The ellipsometer fit of the model to the data for complete metamaterial, tuned to the Dirac Point. The fit MSE was 9.512.

## TUNING THE DISPERSION OF ANISOTROPIC 2D MATERIALS WITH GRAPHENE

Graphene/black phosphorus (BP) heterostructures are used as a platform for exploring tunable anisotropic dispersion. The biaxial anisotropic nature and negative permittivity, coupled with the graphene tunability present an opportunity for tuning 2D hyperbolic heterostructures. We show a proposed design for a tunable epsilon near zero behavior that allows for beam steering.

### 4.1 Introduction

Having demonstrated in the previous chapter the viability of tuning the permittivity of bulk dielectrics, we move on to more exotic materials. Van der Waals materials beyond graphene have attracted considerable interest [107]. In particular, there exist naturally hyperbolic 2D materials such as black phosphorus and MoO<sub>3</sub> [108, 109]. By placing graphene near these materials, we aim to affect the local dielectric environment by tuning the carrier concentration in graphene. Hyperbolic materials have been shown to exhibit beam steering properties [110, 111] owing to their unique dispersion relation.

### 4.2 Properties of black phosphorus

Black phosphorus (BP) is a semiconducting allotrope of phosphorus that forms layers. These sheets are stacked on top of each other, forming the bulk material with a bandgap of 0.3eV. By mechanical exfoliation, it is possible to isolate a single sheet. Without the layer-to-layer coupling of the bulk material, the bandgap of a single layer of BP rises to 2eV. Each phosphorus atom bonded to its three neighbors [112]. These sp<sup>3</sup> hybridized bonds bend the phosphorus into a puckered shape, with distinct behavior along the armchair and zig-zag axis. This geometry creates an anisotropic dielectric response, allowing BP to act as a hyperbolic material [113]. Similarly to graphene, the charge concentration in BP can be controlled by an electrostatic gate.

The natural birefringence of BP make it an intriguing candidate for polarization control and beam steering. There exist a library of other naturally hyperbolic materials [114]. However, BP is a particularly interesting material, as it is an

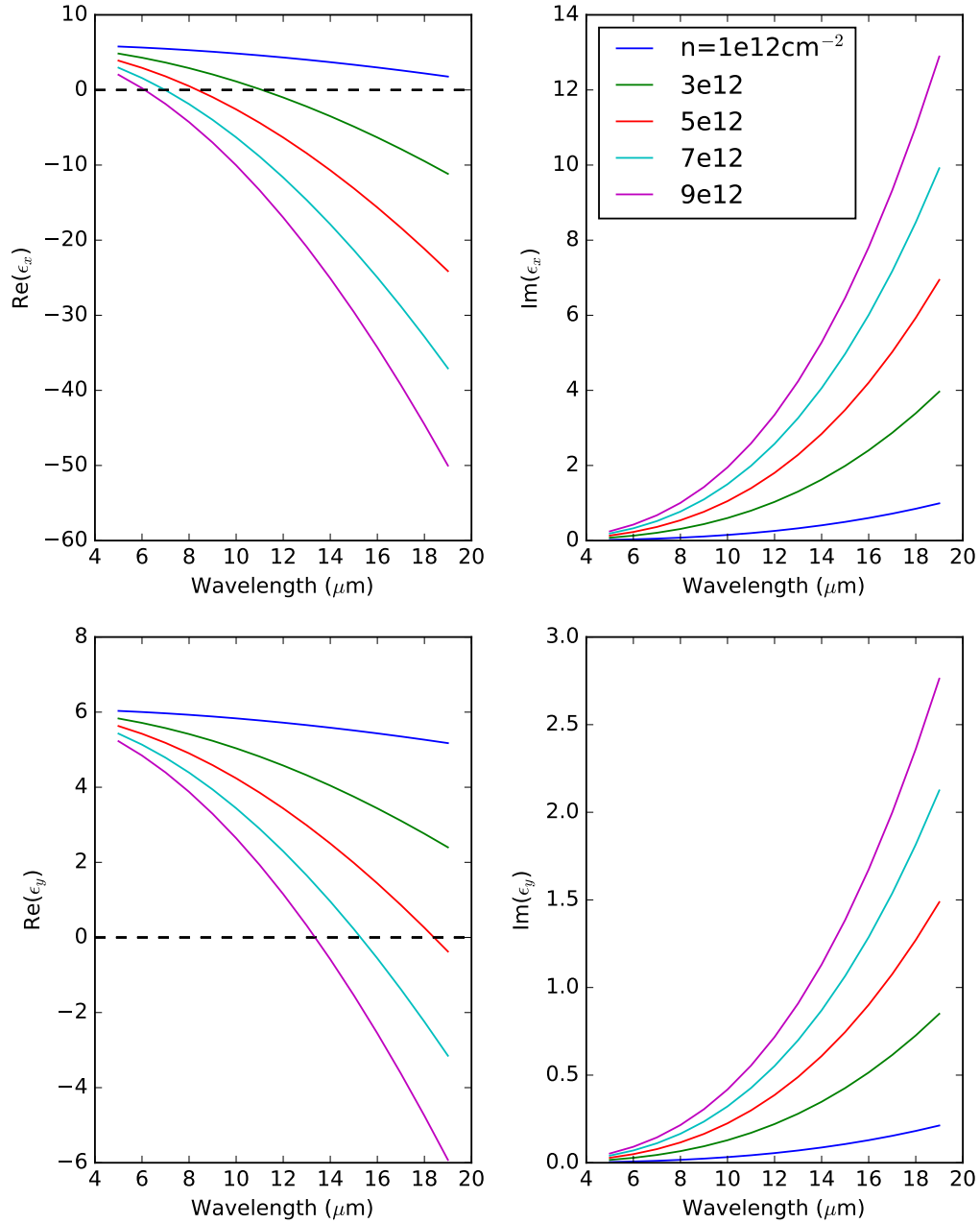


Figure 4.1: The in-plane permittivity of black phosphorus[113].  $n$  is the carrier concentration. It exhibits tunable ENZ points.

electrostatically tunable 2D material.

### 4.3 Permittivity of BP

The permittivity of BP is anisotropic. For electrons, the effective mass is  $m_{cx} = 0.15m_0$ .  $m_{cy} = 0.07m_0$ , where  $x$  is in the zig zag direction and  $y$  is in the zig-zag

direction. The region of interest in this work is the mid to far-infrared as that is the region of tunability over which BP crosses  $Re(\epsilon) = 0$ . We follow Tony Low's Kubo method for calculating the permittivity of BP [113].

Along the direction  $j$ , we can calculate the Drude weight  $D_j$

$$D_j = \pi e^2 n / m_{c_j}. \quad (4.1)$$

This value can be used to calculate the optical conductivity.

$$\sigma_j = \frac{iD_j}{\pi(\omega + i\eta/\hbar)}. \quad (4.2)$$

The value of  $\eta$  can be calculated from the scattering time of BP. Typical values are near 10meV, but this value depends on the quality of the BP. We can use optical conductivity to calculate the permittivity.

$$\epsilon_j = \epsilon_r + \frac{i\sigma_j}{\omega\Delta t\epsilon_0}. \quad (4.3)$$

This permittivity follows that of classic plasmon dispersion, with movement in each direction being affected by the different effective masses in each direction.

#### 4.4 Properties of hBN

Hexagonal boron nitride is another material of interest. It is a 2D material that acts as an insulator, allowing for separation between other 2D materials at different charge concentrations. It has an in-plane phonon at  $13.1\mu m$  and an out-of-plane phonon at  $7.4\mu m$ . It is also a hyperbolic metamaterial in the reststrahlen bands from  $13.2-12.1\mu m$  and  $6.27-7.35\mu m$ . [115, 116].

#### 4.5 Design of a Graphene/BP Heterostructure

The heterostructure [see Fig. 4.2] is as follows: There is a silicon substrate with a thick top layer of  $Al_2O_3$ . On that is transferred a layer of graphene. On this is a layer of hBN, then a layer of BP, then a layer of hBN. hBN is used to insulate the graphene from the black phosphorus, allowing the two materials to be gated against each other and have different carrier concentrations.

By placing graphene near the BP, we can change the response of the overall structure, allowing us to tune the hyperbolic behavior.

#### 4.6 Effective permittivity

To calculate the theoretical behavior of the device we use effective medium theory. In plane, the permittivity is related to the  $\epsilon$  of the nearby materials 1 and 2. [117,

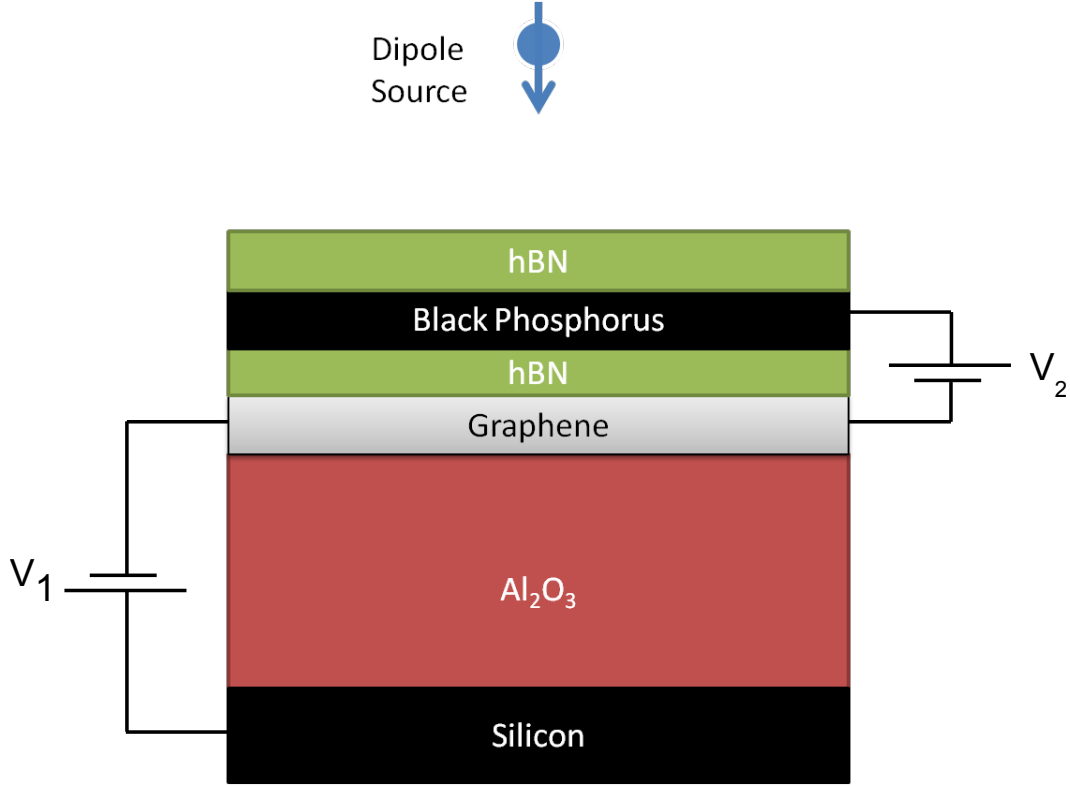


Figure 4.2: A source above the graphene BP heterostructure excites in-plane plasmons. The graphene and BP are separated by a layer of hBN. Voltages  $V_1$  and  $V_2$  can be applied to electrostatically gate the graphene and BP.

118, 119]

$$\epsilon_{||} = \rho\epsilon_{||1} + (1 - \rho)\epsilon_{||2}, \quad (4.4)$$

$$\epsilon_{\perp} = [\rho\epsilon_{\perp1}^{-1} + (1 - \rho)\epsilon_{\perp2}^{-1}]^{-1}. \quad (4.5)$$

From effective medium theory, we can calculate the effective permittivities of the structure [see Fig. 4.3]. There are different crossings of  $Re(\epsilon_x, y) = 0$  at different wavelengths. This effect is due to the anisotropy of the underlying materials. The local environment plays a factor in the effective index that the plasmon interacts with, so care needs to be taken to avoid phonons in the regions of interest.

Once we have an effective medium, we can vary the properties of the tunable materials. If we change the Fermi level of the graphene, we can change the crossing point of the  $Re(\epsilon_x, y) = 0$  [see Fig. 4.4].

By separately tuning the doping of BP, [see Fig. 4.5], we allow an additional degree of freedom in changing the permittivity of the material. Therefore, at a

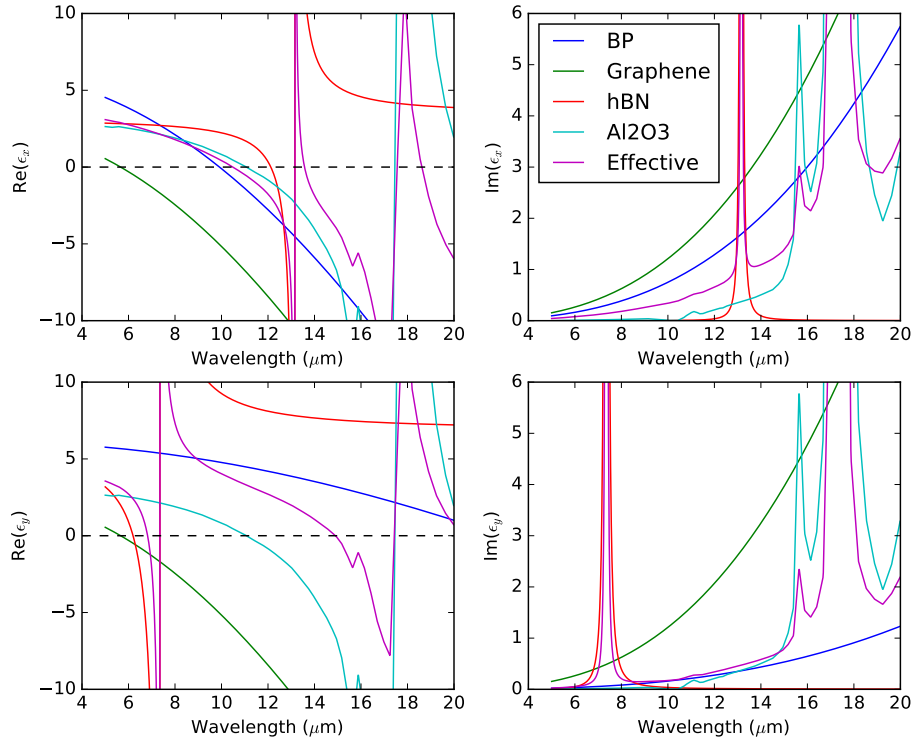


Figure 4.3: The in-plane permittivities of the materials in the heterostructure and their effective permittivity. This structure is graphene at  $E_f=0.1\text{eV}$ , 5 nm of hBN, 10 nm of BP with a carrier concentration  $5e12$ , and 5 nm of hBN.

given wavelength, we have two degrees of freedom, graphene  $E_f$  and BP carrier concentration, and two values we want to control,  $Re(\epsilon_x)$  and  $Re(\epsilon_y)$ .

#### 4.7 Near-field imaging of isofrequency contours

A technique for measuring hyperbolic dispersion uses the tip of an scanning near-field optical microscope (s-NSOM) to stimulate plasmon modes [120]. The tip both acts to stimulate plasmons and collect the reflected field from the edges of the flake. To simulate this using FDTD, we place a dipole source at a height  $h$  above the surface. In an experiment, one has places metals around the edge of the flakes so the field can be recovered by the tip and computed. By placing a monitor above the surface of the material, we can record this electric field. Next, we take a Fourier transform of the electric field. This transformation from real space to k-space of the out-of-plane component of the electric field gives the iso-frequency contours of the k-vector dispersion. There exist other methods of imaging isofrequency, such as

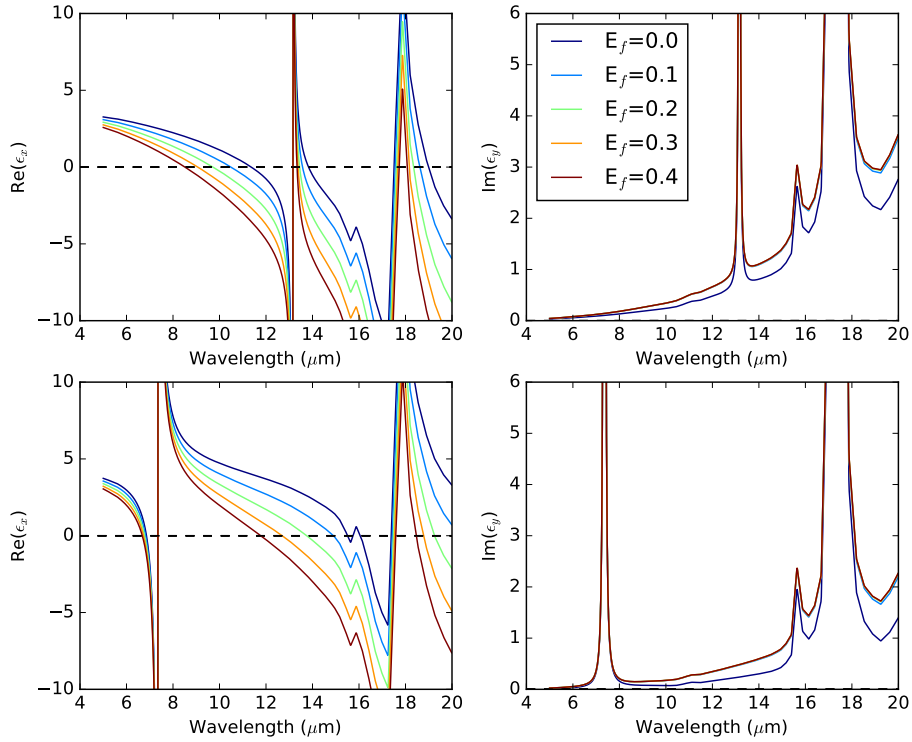


Figure 4.4: The in-plane effective permittivities for a variety of graphene Fermi levels. This structure is graphene with a Fermi level of 0.0 to 0.4V, 5 nm of hBN, 10 nm of BP with a carrier concentration  $5e12$ , and 5 nm of hBN.

back focal plane microscopy [121]. This technique was selected because it has had a proven track record with 2D materials [120].

As the sample has elliptic dispersion regions and hyperbolic dispersion regions, one would expect to be able to see this transition. The angle of the the isofrequency contours is related to the permittivity of the material.

$$\theta(\omega) = \pi/2 - \arctan(\sqrt{\epsilon_y(\omega)}/i\sqrt{\epsilon_x(\omega)}). \quad (4.6)$$

Note that this dispersion relation shows a correlation in the propagation direction. Instead of propagating elliptically, hyperbolic materials will emit in an X shape, as the momentum in the x and y are correlated with each other. This distinctive pattern is characteristic of hyperbolic materials and is a sign of hyperbolic behavior.

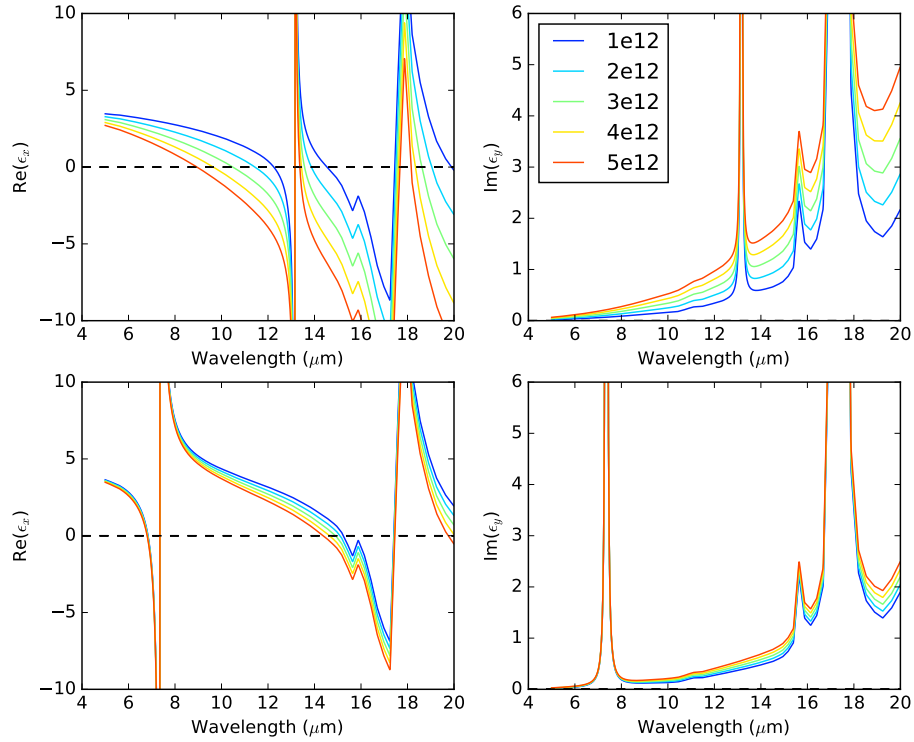


Figure 4.5: The in-plane effective permittivities for a variety of graphene Fermi levels. This structure is graphene with an  $E_f$  of 0.1 eV, 5 nm of hBN, 10 nm of BP with a carrier concentration varying from  $1e12$  to  $9e12$ , and 5 nm of hBN.

#### 4.8 FDTD Simulations

To simulate the structure, we perform FDTD simulations using Lumerical, a commercial software package. We ran the simulation [See Table 4.1] and performed the Fourier transform to recover the isofrequencies [see Fig. 4.6]. Our effective media theory approach roughly captures the behavior of the heterostructure. As bias is applied to the graphene, the permittivity shifts, resulting in a change in the isofrequencies.

By comparing the Fourier transformed image and real space image of the electric field [see Fig. 4.7], we can see propagation of energy in the direction of the hyperbolic dispersion. From Fig. 4.8, we can see that the bulk of the mode is in the BP. As we are taking a cross section of the profile at a distance, the two lobes we see are a cross section of the X-shaped radiation pattern.

From the effective permittivities of the heterostructure, we calculate the beam steer-

Simulation region spane in plane	$2\mu\text{m}$ by $2\mu\text{m}$
Simulation region spane in plane	$4.5\mu\text{m}$
Out of plane mesh size cell3	1 nm
In plane mesh size cell6	1 nm
Out of plane mesh span	100 nm
In plane mesh span	2000 nm
Gold ring inner diameter	800 nm
BP thickness	10 nm
hBN thicknees	5 nm

Table 4.1: FDTD Simulation Parameters Fig. 4.6

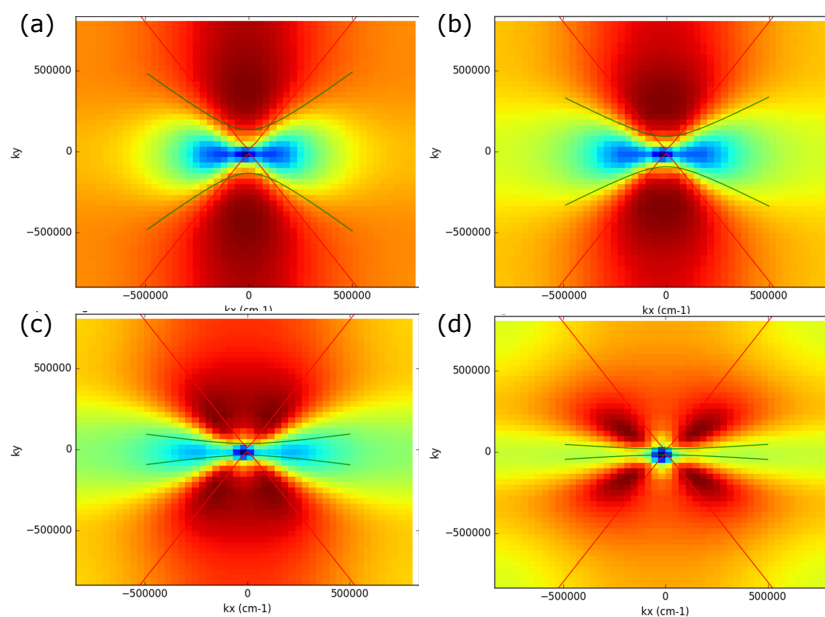


Figure 4.6: The isofrequency curves of the simulation at  $12\mu\text{m}$  The  $E_f$  is 0.04 eV in (a) and increased up to 0.1 eV in (d). The red line is the dispersion of the BP and the green line is the dispersion of the heterostructure as a whole. As the the bias is applied, the area of isofrequencies flatten and expand as the isofrequency curves become more horizontal.

ing of the device[see Fig. 4.9]. The energy propagates in four directions with  $D_2$  symmetry.

#### 4.9 Biaxial effective parameter retrieval

The theoretical approach here consisted of effective medium theory. This approach could be enhanced through more rigorous methodologies. Effective parameter

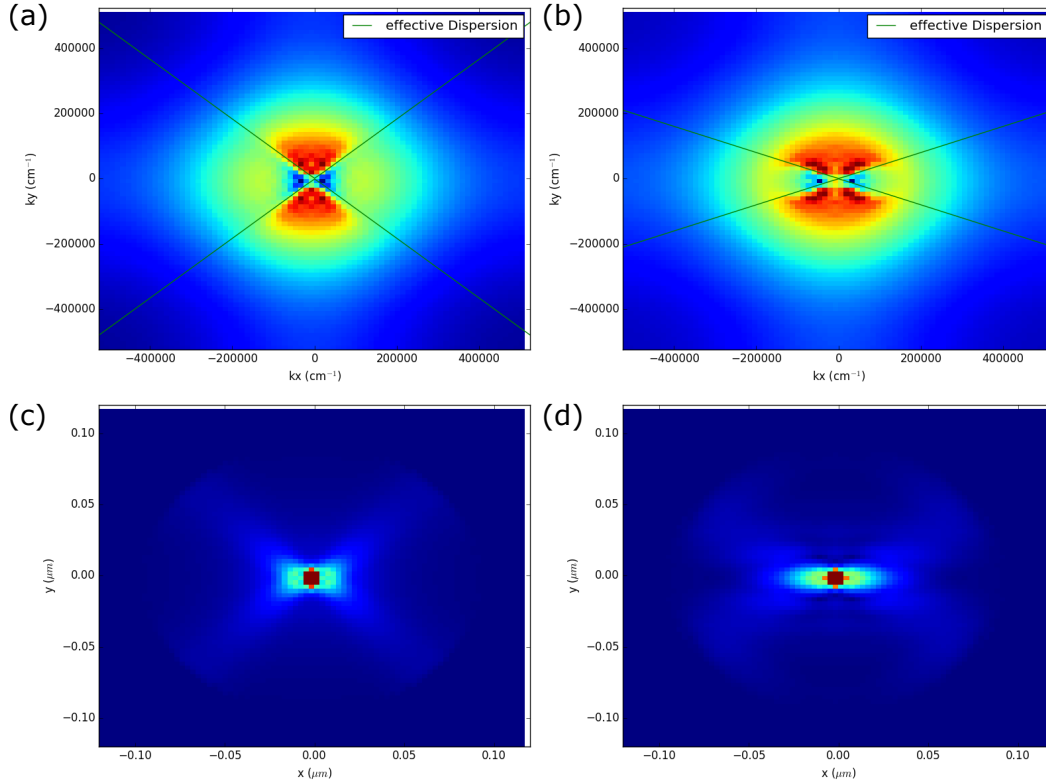


Figure 4.7: (a-b) FFT image of the  $E_z$  of a graphene-BP heterostructure at  $\lambda = 12\mu\text{m}$  with a BP carrier concentration of  $4e12\text{cm}^{-2}$  and a graphene Fermi level of (a) 0.1 eV (b) 0.2 eV. (c-d) Real space image of  $|E|$  of the above, indicating the direction of energy propagation.

retrieval [105] based on transfer matrices would be a more rigorous method to find the permittivity of the material. Current approaches in effective parameter retrieval have been done for uniaxial materials. For biaxial materials, this approach needs to be extended.

A 4x4 transfer matrix approach [104] is needed to calculate the full reflection and transmission characteristics of the metamaterial stack. Rather than depending on a single angle of incidence  $\theta$ , the light is incident at angle  $(\theta, \phi)$ , due to the azimuthal orientation of the heterostructure. The wave breaks into four components rather than two as the s and p polarizations see different effective indexes and propagate with different  $k_z$ . Once the transfer matrices are calculated, they can be used to find the wave parameters  $\epsilon_{TE/TM}(\theta, \psi)$  and  $k_{eff,TE/TM}(\theta, \psi)$ . From these quantities, material parameter retrieval is necessary to find  $\epsilon_{TE/TM}$ . This approach would generate a more accurate value for  $\epsilon$ .

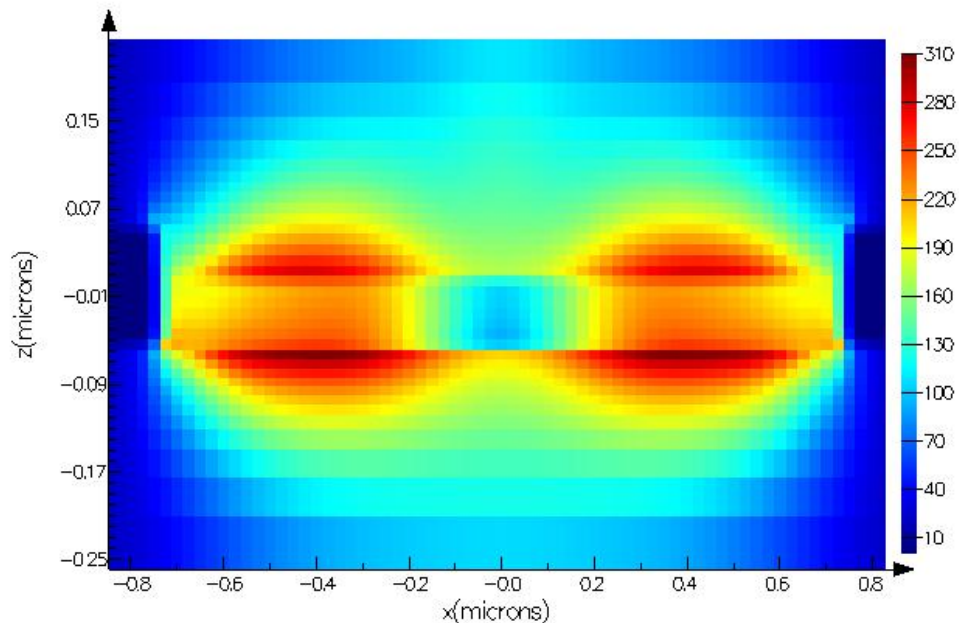


Figure 4.8: The cross-sectional view of the electric field profile of a graphene-BP heterostructure taken 400 nm away from the dipole excitation. Graphene is at -53 nm, and BP is from -50 nm to 0 nm. This image shows that the majority of the power resides in the BP mode, but the highest electric field strength is in the underlying graphene sheet.

#### 4.10 Conclusion

Graphene presents a viable avenue for tuning 2D anisotropic materials. This has applications for beam steering. The advantage a graphene-BP heterostructure is that both materials are tunable, allowing for control of the hyperbolic behavior of the material. Additionally, this approach can be used to tune other materials such as  $\text{MoO}_3$ , which is naturally hyperbolic but not directly tunable via electrostatic gating.

We present a viable device configuration for the measurement of beam steering and hyperbolic behavior by a graphene/BP heterostructure. The device can be fabricated by the mechanical exfoliation of various 2D materials as well as the deposition of contacts by variety of methods. A s-NSOM measurement would be able to show the signature of hyperbolic behavior. Though not experimentally realized at this time, we hope these illustrations will guide future work.

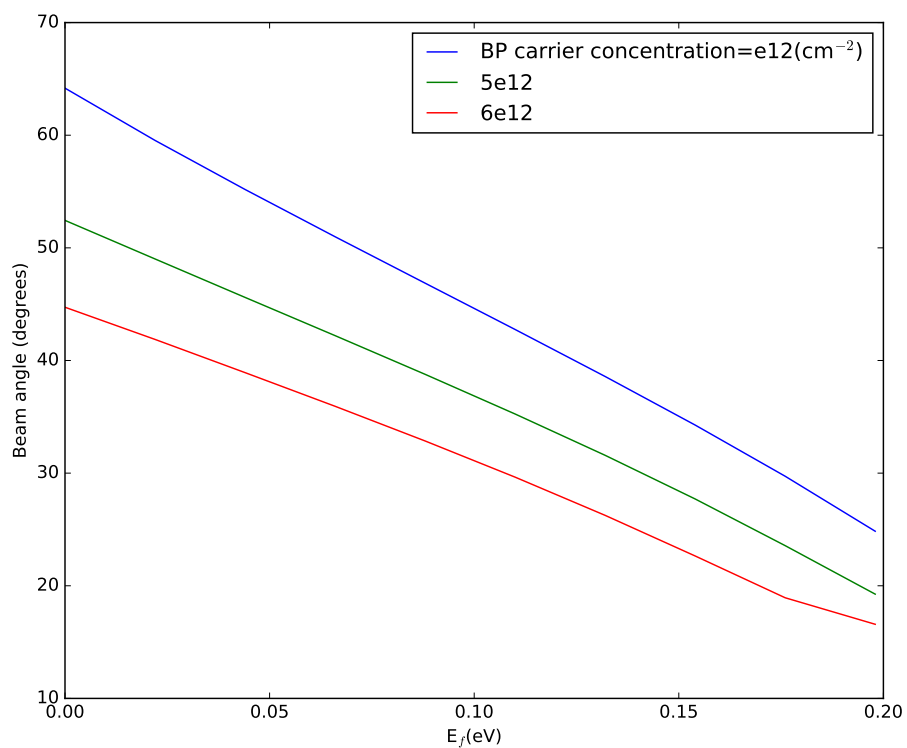


Figure 4.9: Effective medium theory is used to calculate the angle of emission for a graphene-BP heterostructure at  $12 \mu\text{m}$ . The thickness of the BP is 50 nm and is encapsulated in hBN. The graphene Fermi level  $E_f$  can control the beam angle, as can the BP carrier concentration.

## PERSPECTIVES AND FUTURE WORKS

### **5.1 Graphene for light emission**

We have presented a method for having an electrically tunable control of light emission. Much of the research and usage of plasmonics is based on the assumption that plasmons are lossy. This weakness limits the usage for communications and other platforms where efficiency and power are valued. The strengths of plasmonics are in the deeply subwavelength length scales of plasmons and their speed.

By using plasmons to couple to non-radiative transitions, we fundamentally change this dynamic. As the optical losses are irrelevant in the non-radiative transition, we can engineer our way around this central caveat of plasmonics.

Laser materials have been limited by the fundamental material properties. Different crystals, oxides, host materials, and emitters are selected for various applications based on their emission wavelength, radiative lifetime, ease of manufacture, and cost. Various techniques have been employed to tune these various properties, including doping, heat-treatment, sensitization, and strain. A limitation of many of these techniques is that they are set at time of manufacture.

Plasmonics presents a way to break this paradigm. By controlling the lifetime of levels using plasmons, we can have a strong increase in radiative lifetime. This technique could allow for usage of new laser material, as previously unused materials could be made viable by proximity to a plasmonic resonator. Plasmonics will increase the speed of materials, owing to their high plasmonic enhancement.

Graphene has advantages over conventional metals for this application. First, it is a 2D material and is therefore fundamentally extremely thin. This feature enables graphene to confine light to smaller mode volumes than bulk metals. As the Purcell enhancement depends on the mode volume, this feature is advantageous. The high mode confinement also means that many plasmonic resonators can be put in the same subwavelength area. A programmable metasurface composed of graphene-based resonators would have interesting applications.

Another essential quality of graphene is tunability. By having electrically tunable control of lifetime, laser materials can be made to support and suppress population

inversion. With Purcell enhancements on the order of  $10^6$ - $10^7$ , materials with lifetimes on the order of milliseconds would have transition rates on the order of GHz. This possibility opens the door for new types of devices that use the high-speed gating of spontaneous emission rate as a modulation method.

This plasmonic enhancement does have limitations. The same plasmonic emitter that couples to a non-radiative transition could couple to a radiative transition, which could quench emission depending on specifics. In addition, this effect occurs over small length scales, on the order of 10s of nm. Plasmonic fields are closely confined to their host material, and so devices would need to take this limitation into account. The change in behavior of macroscopically thick bulk crystals would be negligible in proximity to graphene. The thickness of the volume of modulation would be a few nanometers thick and would need to be very close to the plasmonic resonator.

We have discovered a novel mechanism for controlling light emission from plasmonics. We show an increase in erbium luminescence by 80%, and 28-fold electrically tunable enhancement of light emission.

## **5.2 Tunable hyperbolic metamaterials**

In developing and fabricating a SiO<sub>2</sub>/graphene heterostructure, we have experimentally demonstrated a device that has been theorized for years. We fabricated a single unit cell of this metamaterial. Extensions to this project could expand to integer multiples of the unit cell. The fabrication process we developed is scalable.

Using graphene sheets on isotropic materials allows for the development of uniaxial effective materials. By being able to separately tune the material in and out of plane, we open the possibility of a tunable elliptic to hyperbolic materials. By being able to tune the density of states from a finite sphere to a hyperboloid, we can enable large Purcell factor enhancement. Hyperbolic materials can be used for sub-diffraction imaging.

Extensions to this process would be to pattern the graphene. A lithography step followed by an oxygen plasma etch can cut ribbons or other structures into the graphene. By breaking the in-plane symmetry of the graphene, we would be able to create a hyperbolic effective medium with biaxial rather than uniaxial symmetry with graphene and conventional dielectrics. Patterning and control of separate elements in a graphene sheet could be used for a metasurface with tunable elliptic to hyperbolic transitions.

### **5.3 Van Der Waals materials beyond graphene**

A recent review paper in Nature[116] proclaims "a wealth of hyperbolic 2D materials await further study." It is an exciting time to be in hyperbolic 2D materials as the library of materials continues to expand and open new possibilities. By utilizing this additional design space, there are other hyperbolic structures. Graphene, as a tunable air-stable material, will be able affect the relative permittivity of stacks of these materials, allowing for the modulation of the exotic optical properties of 2D materials beyond graphene.

### **5.4 Conclusions**

From light emission to transmission and absorption, graphene has a broad range of applications. The high-confinement, extreme Purcell enhancement, and electrostatic tunability contribute to the uses of this material. I have conceived of new uses of plasmonics, built devices that had been theorized for years by numerous researchers, and explored the possibilities of novel tunable hyperbolic 2D materials.

2D materials is a fast-paced field. With the discovery of isolated graphene in 2004 and the Nobel Prize being awarded in 2010, researchers have poured into field. Materials beyond graphene have been discovered and there is continual invention as people fabricate and explore new materials. Plasmonic and hyperbolic materials' strength is in light confinement and it is hard to get thinner than an atom or two. The control of light emission and propagation on tiny length scales is greatly aided by this suite of growing materials. Careful diligent experimentation is needed to realize these devices and turn them into practical improvements. I hope they bring good to the world.

## BIBLIOGRAPHY

- [1] James Clerk Maxwell. “VIII. A dynamical theory of the electromagnetic field”. *Philosophical transactions of the Royal Society of London* 155 (1865), pp. 459–512.
- [2] KS Novoselov. “Nobel lecture: Graphene: Materials in the flatland”. *Reviews of Modern Physics* 83.3 (2011), p. 837.
- [3] Matthew J Allen, Vincent C Tung, and Richard B Kaner. “Honeycomb carbon: a review of graphene”. *Chemical reviews* 110.1 (2009), pp. 132–145.
- [4] Wonbong Choi et al. “Synthesis of graphene and its applications: a review”. *Critical Reviews in Solid State and Materials Sciences* 35.1 (2010), pp. 52–71.
- [5] Roberto Muñoz and Cristina Gómez-Aleixandre. “Review of CVD synthesis of graphene”. *Chemical Vapor Deposition* 19.10-11-12 (2013), pp. 297–322.
- [6] Daniel R Cooper et al. “Experimental review of graphene”. *ISRN Condensed Matter Physics* 2012 (2012).
- [7] Frank Schwierz. “Graphene transistors”. *Nature nanotechnology* 5.7 (2010), p. 487.
- [8] Artur M Pinto, Ines C Goncalves, and Fernao D Magalhaes. “Graphene-based materials biocompatibility: a review”. *Colloids and Surfaces B: Biointerfaces* 111 (2013), pp. 188–202.
- [9] Xin Li et al. “Graphene in photocatalysis: a review”. *Applied Surface Science* 12.48 (2016), pp. 6640–6696.
- [10] Jian Li et al. “Review of electrochemical capacitors based on carbon nanotubes and graphene”. *Graphene* 1.01 (2012), p. 1.
- [11] WK Chee et al. “Flexible graphene-based supercapacitors: a review”. *The Journal of Physical Chemistry C* 120.8 (2016), pp. 4153–4172.
- [12] Eric Singh and Hari Singh Nalwa. “Graphene-based bulk-heterojunction solar cells: a review”. *Journal of nanoscience and nanotechnology* 15.9 (2015), pp. 6237–6278.
- [13] Gints Kucinskis, Gunars Bajars, and Janis Kleperis. “Graphene in lithium ion battery cathode materials: A review”. *Journal of Power Sources* 240 (2013), pp. 66–79.
- [14] Zhao Jing, Zhang Guang-Yu, and Shi Dong-Xia. “Review of graphene-based strain sensors”. *Chinese Physics B* 22.5 (2013), p. 057701.

- [15] Xiaoting Jia et al. “Graphene edges: a review of their fabrication and characterization”. *Nanoscale* 3.1 (2011), pp. 86–95.
- [16] Sudipta Dutta and Swapan K Pati. “Novel properties of graphene nanoribbons: a review”. *Journal of Materials Chemistry* 20.38 (2010), pp. 8207–8223.
- [17] Fancheng Meng et al. “Graphene-based fibers: a review”. *Advanced materials* 27.35 (2015), pp. 5113–5131.
- [18] Chen Si, Zhimei Sun, and Feng Liu. “Strain engineering of graphene: a review”. *Nanoscale* 8.6 (2016), pp. 3207–3217.
- [19] Yan Wang et al. “Two-dimensional thermal transport in graphene: a review of numerical modeling studies. *Nanoscale Microscale Thermophys*”. Eng. Citeseer. 2014.
- [20] Beidou Guo et al. “Graphene doping: a review”. *Insciences J.* 1.2 (2011), pp. 80–89.
- [21] Lili Liu et al. “Defects in graphene: generation, healing, and their effects on the properties of graphene: a review”. *Journal of Materials Science & Technology* 31.6 (2015), pp. 599–606.
- [22] EH Hwang and S Das Sarma. “Dielectric function, screening, and plasmons in two-dimensional graphene”. *Physical Review B* 75.20 (2007), p. 205418.
- [23] Kirill I Bolotin et al. “Ultrahigh electron mobility in suspended graphene”. *Solid State Communications* 146.9-10 (2008), pp. 351–355.
- [24] Tony Low and Phaedon Avouris. “Graphene plasmonics for terahertz to mid-infrared applications”. *ACS nano* 8.2 (2014), pp. 1086–1101.
- [25] AN Grigorenko, Marco Polini, and KS Novoselov. “Graphene plasmonics”. *Nature photonics* 6.11 (2012), p. 749.
- [26] George W Hanson. “Dyadic Green’s functions and guided surface waves for a surface conductivity model of graphene”. *Journal of Applied Physics* 103.6 (2008), p. 064302.
- [27] Jonathan P Dowling. “Spontaneous emission in cavities: How much more classical can you get?” *Foundations of physics* 23.6 (1993), pp. 895–905.
- [28] Edward M Purcell, H Co Torrey, and Robert V Pound. “Resonance absorption by nuclear magnetic moments in a solid”. *Physical review* 69.1-2 (1946), p. 37.
- [29] Victor W Brar et al. “Highly confined tunable mid-infrared plasmonics in graphene nanoresonators”. *Nano letters* 13.6 (2013), pp. 2541–2547.
- [30] DR Smith et al. “Gradient index metamaterials”. *Physical Review E* 71.3 (2005), p. 036609.

- [31] David Schurig et al. “Metamaterial electromagnetic cloak at microwave frequencies”. *Science* 314.5801 (2006), pp. 977–980.
- [32] Wenshan Cai et al. “Optical cloaking with metamaterials”. *Nature photonics* 1.4 (2007), p. 224.
- [33] Shuang Zhang et al. “Plasmon-induced transparency in metamaterials”. *Physical review letters* 101.4 (2008), p. 047401.
- [34] Huanyang Chen, Che Ting Chan, and Ping Sheng. “Transformation optics and metamaterials”. *Nature materials* 9.5 (2010), p. 387.
- [35] VG Veselago. “Electrodynamics of substances with simultaneously negative electrical and magnetic permeabilities”. *Physics-Uspexhi* 10.4 (1968), pp. 504–509.
- [36] Zubin Jacob et al. “Engineering photonic density of states using metamaterials”. *Applied physics B* 100.1 (2010), pp. 215–218.
- [37] Wei Yan, Martijn Wubs, and N Asger Mortensen. “Hyperbolic metamaterials: nonlocal response regularizes broadband supersingularity”. *Physical Review B* 86.20 (2012), p. 205429.
- [38] Lorenzo Ferrari et al. “Hyperbolic metamaterials and their applications”. *Progress in Quantum Electronics* 40 (2015), pp. 1–40.
- [39] CL Cortes et al. “Quantum nanophotonics using hyperbolic metamaterials”. *Journal of Optics* 14.6 (2012), p. 063001.
- [40] Zhiwei Guo et al. “Actively controlling the topological transition of dispersion based on electrically controllable metamaterials”. *Applied Sciences* 8.4 (2018), p. 596.
- [41] RH Ritchie. “Surface plasmons in solids”. *Surface Science* 34.1 (1973), pp. 1–19.
- [42] MA Noginov et al. “Controlling spontaneous emission with metamaterials”. *Optics letters* 35.11 (2010), pp. 1863–1865.
- [43] Andreas Brenneis et al. “Ultrafast electronic readout of diamond nitrogen–vacancy centres coupled to graphene”. *Nature nanotechnology* 10.2 (2015), p. 135.
- [44] LA Blanco and FJ Garcia De Abajo. “Spontaneous light emission in complex nanostructures”. *Physical review B* 69.20 (2004), p. 205414.
- [45] A Yu Nikitin et al. “Fields radiated by a nanoemitter in a graphene sheet”. *Physical Review B* 84.19 (2011), p. 195446.
- [46] Thang B Hoang et al. “Ultrafast spontaneous emission source using plasmonic nanoantennas”. *Nature Communications* 6 (2015), p. 7788.
- [47] KJ Tielrooij et al. “Electrical control of optical emitter relaxation pathways enabled by graphene”. *Nature Physics* 11.3 (2015), p. 281.

- [48] Nicholas Rivera et al. “Shrinking light to allow forbidden transitions on the atomic scale”. *Science* 353.6296 (2016), pp. 263–269.
- [49] Hugen Yan et al. “Damping pathways of mid-infrared plasmons in graphene nanostructures”. *Nature Photonics* 7.5 (2013), p. 394.
- [50] Zheyuan Chen et al. “Energy transfer from individual semiconductor nanocrystals to graphene”. *ACS nano* 4.5 (2010), pp. 2964–2968.
- [51] Dmitri K Gramotnev and Sergey I Bozhevolnyi. “Plasmonics beyond the diffraction limit”. *Nature photonics* 4.2 (2010), p. 83.
- [52] MA Noginov et al. “Compensation of loss in propagating surface plasmon polariton by gain in adjacent dielectric medium”. *Optics express* 16.2 (2008), pp. 1385–1392.
- [53] MA Noginov et al. “The effect of gain and absorption on surface plasmons in metal nanoparticles”. *Applied Physics B* 86.3 (2007), pp. 455–460.
- [54] ES Andrianov et al. “Loss compensation by spasers in plasmonic systems”. *Optics express* 21.11 (2013), pp. 13467–13478.
- [55] Anan Fang, Thomas Koschny, and Costas M Soukoulis. “Lasing in meta-material nanostructures”. *Journal of optics* 12.2 (2010), p. 024013.
- [56] J\_ Seidel, S Grafström, and L Eng. “Stimulated emission of surface plasmons at the interface between a silver film and an optically pumped dye solution”. *Physical review letters* 94.17 (2005), p. 177401.
- [57] Sergey Bozhevolnyi. *Plasmonic nanoguides and circuits*. Pan Stanford, 2008.
- [58] C Randy Giles and Emmanuel Desurvire. “Modeling erbium-doped fiber amplifiers”. *Journal of lightwave technology* 9.2 (1991), pp. 271–283.
- [59] Paul Urquhart. “Review of rare earth doped fibre lasers and amplifiers”. *IEE Proceedings J (Optoelectronics)* 135.6 (1988), pp. 385–407.
- [60] Phillip A Burns et al. “Optimization of Er, Yb: YCOB for CW laser operation”. *IEEE journal of quantum electronics* 40.11 (2004), pp. 1575–1582.
- [61] Trinh Tu Van and Jane P Chang. “Controlled erbium incorporation and photoluminescence of Er-doped Y<sub>2</sub>O<sub>3</sub>”. *Applied Physics Letters* 1 (2005), p. 011907.
- [62] Yutaka Nigara. “Measurement of the optical constants of yttrium oxide”. *Japanese Journal of Applied Physics* 7.4 (1968), p. 404.
- [63] T Sanamyan et al. “High power diode-pumped 2.7- $\mu\text{m}$  Er<sup>3+</sup>: Y<sub>2</sub>O<sub>3</sub> laser with nearly quantum defect-limited efficiency”. *Optics express* 19.105 (2011), A1082–A1087.
- [64] T Sanamyan. “Diode pumped cascade Er: Y<sub>2</sub>O<sub>3</sub> laser”. *Laser Physics Letters* 12.12 (2015), p. 125804.

- [65] Min Seok Jang et al. “Tunable large resonant absorption in a midinfrared graphene Salisbury screen”. *Physical Review B* 90.16 (2014), p. 165409.
- [66] Lukas Novotny and Bert Hecht. *Principles of nano-optics*. Cambridge university press, 2012.
- [67] Marlan O. Scully and M. Suhail Zubairy. *Quantum Optics*. Cambridge University Press, 1997. DOI: 10.1017/CBO9780511813993.
- [68] Ulrike Woggon. *Optical properties of semiconductor quantum dots*. Vol. 136. Springer, 1997.
- [69] Hai xia Ma et al. “5.5 W CW Yb<sup>3+</sup>: Y<sub>2</sub>O<sub>3</sub> ceramic laser pumped with 970 nm laser diode”. *Optics communications* 246.4-6 (2005), pp. 465–469.
- [70] Dylan Lu et al. “Enhancing spontaneous emission rates of molecules using nanopatterned multilayer hyperbolic metamaterials”. *Nature nanotechnology* 9.1 (2014), p. 48.
- [71] Jing Zhou et al. “Experiment and theory of the broadband absorption by a tapered hyperbolic metamaterial array”. *ACS photonics* 1.7 (2014), pp. 618–624.
- [72] Ruben Maas et al. “Experimental realization of an epsilon-near-zero metamaterial at visible wavelengths”. *Nature Photonics* 7.11 (2013), p. 907.
- [73] Ahmed M Mahmoud and Nader Engheta. “Wave-matter interactions in epsilon-and-mu-near-zero structures”. *Nature Communications* 5 (2014), p. 5638.
- [74] Nader Engheta. “Pursuing near-zero response”. *Science* 340.6130 (2013), pp. 286–287.
- [75] John Brian Pendry. “Negative refraction makes a perfect lens”. *Physical review letters* 85.18 (2000), p. 3966.
- [76] Cristian L Cortes, Matthew Otten, and Stephen K Gray. “Ground-state cooling enabled by critical coupling and dark entangled states”. *Physical Review B* 99.1 (2019), p. 014107.
- [77] Muhan Choi et al. “A terahertz metamaterial with unnaturally high refractive index”. *Nature* 470.7334 (2011), p. 369.
- [78] Daniel S Weile. “Electromagnetic Metamaterials: Physics and Engineering Explorations (Engheta, N. and Ziolkowski, RW; 2006)[Book Review]”. *IEEE Antennas and Propagation Magazine* 49.4 (2007), pp. 137–139.
- [79] Kostya S Novoselov et al. “Two-dimensional gas of massless Dirac fermions in graphene”. *nature* 438.7065 (2005), p. 197.
- [80] David R Andersen. “Graphene-based long-wave infrared TM surface plasmon modulator”. *JOSA B* 27.4 (2010), pp. 818–823.

- [81] Ashkan Vakil and Nader Engheta. “Transformation optics using graphene”. *Science* 332.6035 (2011), pp. 1291–1294.
- [82] Marco Polini et al. “Plasmons and the spectral function of graphene”. *Physical Review B* 77.8 (2008), p. 081411.
- [83] Alexander Poddubny et al. “Hyperbolic metamaterials”. *Nature Photonics* 7.12 (2013), p. 948.
- [84] Ivan V Iorsh et al. “Hyperbolic metamaterials based on multilayer graphene structures”. *Physical Review B* 87.7 (2013), p. 075416.
- [85] Mohamed AK Othman, Caner Guclu, and Filippo Capolino. “Graphene–dielectric composite metamaterials: evolution from elliptic to hyperbolic wavevector dispersion and the transverse epsilon-near-zero condition”. *Journal of Nanophotonics* 7.1 (2013), p. 073089.
- [86] Jacob Linder and Klaus Halterman. “Graphene-based extremely wide-angle tunable metamaterial absorber”. *Scientific reports* 6 (2016), p. 31225.
- [87] Andrei Andryieuski and Andrei V Lavrinenko. “Graphene metamaterials based tunable terahertz absorber: effective surface conductivity approach”. *Optics express* 21.7 (2013), pp. 9144–9155.
- [88] Han Xiong et al. “Ultra-thin and broadband tunable metamaterial graphene absorber”. *Optics express* 26.2 (2018), pp. 1681–1688.
- [89] SH Zainud-Deen, AM Mabrouk, and HA Malhat. “Frequency tunable graphene metamaterial reflectarray”. *2017 XXXIIInd General Assembly and Scientific Symposium of the International Union of Radio Science (URSI GASS)*. IEEE. 2017, pp. 1–4.
- [90] Ashley M DaSilva et al. “Enhancement of photonic density of states in finite graphene multilayers”. *Physical Review B* 88.19 (2013), p. 195411.
- [91] Tian Zhang, Lin Chen, and Xun Li. “Graphene-based tunable broadband hyperlens for far-field subdiffraction imaging at mid-infrared frequencies”. *Optics express* 21.18 (2013), pp. 20888–20899.
- [92] Sarang Pendharker et al. “Thermal graphene metamaterials and epsilon-near-zero high temperature plasmonics”. *Journal of Optics* 19.5 (2017), p. 055101.
- [93] Pavel N Dyachenko et al. “Controlling thermal emission with refractory epsilon-near-zero metamaterials via topological transitions”. *Nature communications* 7 (2016), p. 11809.
- [94] Michaël Lobet et al. “Perfect electromagnetic absorption using graphene and epsilon-near-zero metamaterials”. *Physical Review B* 93.23 (2016), p. 235424.

- [95] Ayed Al Sayem et al. “Control of reflection through epsilon near zero graphene based anisotropic metamaterial”. *8th International Conference on Electrical and Computer Engineering*. IEEE. 2014, pp. 812–815.
- [96] You-Chia Chang et al. “Realization of mid-infrared graphene hyperbolic metamaterials”. *Nature communications* 7 (2016), p. 10568.
- [97] Isaac John Luxmoore et al. “Strong coupling in the far-infrared between graphene plasmons and the surface optical phonons of silicon dioxide”. *ACS photonics* 1.11 (2014), pp. 1151–1155.
- [98] Daniel Q McNerny et al. “Direct fabrication of graphene on SiO<sub>2</sub> enabled by thin film stress engineering”. *Scientific reports* 4 (2014), p. 5049.
- [99] Jae S Park et al. “Wetting and evaporative aggregation of nanofluid droplets on CVD-synthesized hydrophobic graphene surfaces”. *Langmuir* 30.28 (2014), pp. 8268–8275.
- [100] B Lee et al. “Characteristics of high-k Al<sub>2</sub>O<sub>3</sub> dielectric using ozone-based atomic layer deposition for dual-gated graphene devices”. *Applied Physics Letters* 97.4 (2010), p. 043107.
- [101] Seyoung Kim et al. “Realization of a high mobility dual-gated graphene field-effect transistor with Al<sub>2</sub>O<sub>3</sub> dielectric”. *Applied Physics Letters* 94.6 (2009), p. 062107.
- [102] LA Falkovsky. “Optical properties of graphene”. *Journal of Physics: Conference Series*. Vol. 129. 1. IOP Publishing. 2008, p. 012004.
- [103] Georgia Theano Papadakis. “Optical Response in Planar Heterostructures: From Artificial Magnetism to Angstrom-Scale Metamaterials”. PhD thesis. California Institute of Technology, 2018.
- [104] A Pochi Yeh. *Optical Waves In Layered Media*. 1988.
- [105] Georgia T Papadakis, Pochi Yeh, and Harry A Atwater. “Retrieval of material parameters for uniaxial metamaterials”. *Physical Review B* 91.15 (2015), p. 155406.
- [106] Xin Wu et al. “Graphene and Graphene-Based Nanomaterials for DNA Detection: A Review”. *Molecules* 23.8 (2018), p. 2050.
- [107] Saptarshi Das et al. “Beyond graphene: progress in novel two-dimensional materials and van der Waals solids”. *Annual Review of Materials Research* 45 (2015), pp. 1–27.
- [108] Xianglian Song et al. “Biaxial hyperbolic metamaterials using anisotropic few-layer black phosphorus”. *Optics express* 26.5 (2018), pp. 5469–5477.
- [109] Edo van Veen et al. “Tuning 2D hyperbolic plasmons in black phosphorus”. *arXiv preprint arXiv:1812.03062* (2018).

- [110] Siyuan Dai et al. “Manipulation and steering of hyperbolic surface polaritons in hexagonal boron nitride”. *Advanced Materials* 30.16 (2018), p. 1706358.
- [111] JS Gomez-Diaz and Andrea Alu. “Flatland optics with hyperbolic metasurfaces”. *ACS Photonics* 3.12 (2016), pp. 2211–2224.
- [112] AS Rodin, A Carvalho, and AH Castro Neto. “Strain-induced gap modification in black phosphorus”. *Physical review letters* 112.17 (2014), p. 176801.
- [113] Tony Low et al. “Plasmons and screening in monolayer and multilayer black phosphorus”. *Physical review letters* 113.10 (2014), p. 106802.
- [114] Karolina Korzeb, Marcin Gajc, and Dorota Anna Pawlak. “Compendium of natural hyperbolic materials”. *Optics express* 23.20 (2015), pp. 25406–25424.
- [115] Joshua D Caldwell et al. “Sub-diffractive volume-confined polaritons in the natural hyperbolic material hexagonal boron nitride”. *Nature communications* 5 (2014), p. 5221.
- [116] Tony Low et al. “Polaritons in layered two-dimensional materials”. *Nature materials* 16.2 (2017), p. 182.
- [117] Omar Kidwai, Sergei V Zhukovsky, and JE Sipe. “Effective-medium approach to planar multilayer hyperbolic metamaterials: Strengths and limitations”. *Physical Review A* 85.5 (2012), p. 053842.
- [118] Xiujuan Zhang and Ying Wu. “Effective medium theory for anisotropic metamaterials”. *Scientific reports* 5 (2015), p. 7892.
- [119] B Wood, JB Pendry, and DP Tsai. “Directed subwavelength imaging using a layered metal-dielectric system”. *Physical Review B* 74.11 (2006), p. 115116.
- [120] Weiliang Ma et al. “In-plane anisotropic and ultra-low-loss polaritons in a natural van der Waals crystal”. *Nature* 562.7728 (2018), p. 557.
- [121] Pidgayko Dmitry et al. “Direct imaging of isofrequency contours in all-dielectric optical metasurface”. *Journal of Physics: Conference Series*. Vol. 1092. 1. IOP Publishing. 2018, p. 012116.